

Neutron Scattering Studies of Magnetic and Non- Magnetic Correlated Systems

Xiao Hu

Suzhou, Jiangsu, China

Bachelor of Science in Physics, Nanjing University, June 2016

A Dissertation presented to the Graduate Faculty of the University of Virginia in

Candidacy for the Degree of Doctor of Philosophy

Department of Physics

University of Virginia

November 2021

Committee Members:

Prof. Seung-Hun Lee

Prof. Israel Klich

Prof. Gia-Wei Chern

Prof. Joshua J. Choi

Abstract

The field of correlated electron systems has been one of the most widely studied areas of research in condensed-matter physics. Due to the Coulomb interactions between electrons in these systems, the collective states cannot be understood via one-electron approximation that one electron is embedded in a static mean field generated by other electrons. To theoretically describe correlated electron systems, the Hubbard model was proposed based on the tight-binding approximation from condensed-matter physics, which describes particles in a periodic potential. According to the ratio of the hopping integral t and on-site interaction U defined in the Hubbard model, correlated electron systems can be categorized as strongly and weakly correlated systems.

For this thesis, we have performed elastic and inelastic neutron scattering measurements on one strongly correlated magnetic system, $\text{Sr}_2\text{CuTe}_{0.5}\text{W}_{0.5}\text{O}_6$, and two weakly correlated non-magnetic systems, $(\text{BA})_2\text{PbI}_4$ (butylammonium lead iodide) and $(\text{PEA})_2\text{PbI}_4$ (phenethyl-ammonium lead iodide).

For $\text{Sr}_2\text{CuTe}_{0.5}\text{W}_{0.5}\text{O}_6$, using sub-K temperature and $20 \mu\text{eV}$ energy resolution neutron scattering experiments, we show that the system below $T_f = 1.7(1)$ K exhibits an extremely weak frozen moment of $\langle S \rangle / S \sim 0.1$. Below T_f the imaginary part of the dynamical susceptibility, $\chi''(\hbar\omega)$, behaves linearly with $\hbar\omega$ for $\hbar\omega < k_B T_f$ where k_B is the Boltzmann constant with the characteristic spin relaxation rate increasing with decreasing temperatures. Above T_f , $\chi''(\hbar\omega)$ behaves as $\tan^{-1}(\hbar\omega/\Gamma_{min})$ at low energies indicating the presence of a distribution of the spin relaxation rate with the lower limit

Γ_{min} , which behaves as a power law with temperature, $\Gamma_{min}/|J| = \left(\frac{k_B T}{|J|}\right)^\alpha$, with $|J| \sim 9$ meV and $\alpha = 1.3(1)$. On the other hand, the spatial spin correlations are two-dimensional and short-range with an in-plane correlation length of $\xi \sim \sqrt{2} d_{NN}$, where d_{NN} is the distance between the nearest-neighbor spins. Our results indicate that $\text{Sr}_2\text{CuTe}_{0.5}\text{W}_{0.5}\text{O}_6$ transits from a gapless disorder-induced spin liquid to a new quantum state below T_f , exhibiting a weak frozen moment and low energy dynamic susceptibility that is linear in energy consistent with a Halperin-Saslow-like excitation which is surprising for such a weak freezing in this highly fluctuating quantum regime.

For the two non-magnetic weakly correlated systems, $(\text{BA})_2\text{PbI}_4$ (butylammonium lead iodide) and $(\text{PEA})_2\text{PbI}_4$ (phenethyl-ammonium lead iodide), by performing temperature-dependent wide energy-range (up to 600 meV) inelastic neutron scattering measurements and density-functional-theory (DFT) calculations, we identified the vibrational dynamics of both samples. We categorized their phonon modes into three different types based on the vibrational energy fractions of different atoms: inorganic modes (which consist of vibrational motions mostly of Pb and I), organic modes (which describe the vibrational motions of organic molecules), and hybrid modes (coupled vibrational motions between Pb-I network and organic molecules).

With the help of quasi-elastic neutron scattering technique and group theory analysis, we characterized the rotational motions of organic molecules in both samples. In $(\text{BA})_2\text{PbI}_4$, two types of rotational modes were revealed: the three-fold (C_3) rotational modes of NH_3 and CH_3 groups; and the four-fold (C_4) rotational mode of the entire molecule about the crystallographic c -axis, which only gets activated in its high-

temperature structural phase ($T > 275$ K). Whereas in $(\text{PEA})_2\text{PbI}_4$, only the C_3 rotational of the NH_3 group was identified.

Based on the characterized rotational dynamics of both samples, we determined and separated the rotational contributions from the measured phonon intensities. We find that the low-energy inorganic modes of both samples have similar scattering intensities and temperature dependence, which is consistent with the fact that regardless of the different organic molecule configurations, the Pb-I networks of both samples are similar and hence the vibrational responses to the incident neutrons are expected to be similar. On the other hand, the scattering intensities of hybrid modes are quite different for the two samples. The much lower intensities of hybrid modes in $(\text{PEA})_2\text{PbI}_4$ than in $(\text{BA})_2\text{PbI}_4$ suggests that the tight stacking of PEA^+ cations probably restrict their vibrational degrees of freedom and hence suppresses the vibrational response of hybrid modes to the incident neutrons. The temperature dependence of either inorganic phonon modes or hybrid phonon modes does not show predominant correlations with photoluminescence quantum yield (PLQY) indicated by their bromide equivalents that we assume to be similar with or same as the iodides. However, the rotational dynamics exhibits an excellent correspondence to PLQY that: below ~ 150 K when the rotational dynamics of both samples are frozen, both of their bromide equivalents' PLQY stay at high levels ($> 90\%$); while above 150 K, the rotational motion of organic molecules in $(\text{BA})_2\text{PbI}_4$ get enhanced much faster than that in $(\text{PEA})_2\text{PbI}_4$, which coincides with the faster decay of PLQY observed in $(\text{BA})_2\text{PbBr}_4$. This correspondence indicates that the rotational dynamics of organic molecules in 2D HOIPs may dominate the optoelectronic performance such as PLQY.

Author's Biographical Sketch

Xiao Hu was born in Suzhou, Jiangsu Province, China. He started his study in physics at Nanjing University in 2012, and then received the Bachelor of Science degree in 2016. In August 2016, he moved to Charlottesville, Virginia, United States, where he continued his study and research as a graduate student in the Department of Physics, University of Virginia. Then in the summer of 2017, he joined Prof. Seung-Hun Lee's group as a Ph. D. candidate. In Prof. Lee's group, he studied crystal structures, rotational, vibrational dynamics, and optoelectronic properties of two-dimensional metal halide perovskites, as well as exotic behaviors in magnetic materials, such as spin freezing and spin fluctuations in frustrated magnets.

Acknowledgements

Firstly, I would like to express my sincere gratitude to Prof. Seung-Hun Lee, my Ph. D. advisor, for his continuous support of my study and research. He helped me throughout my Ph. D. period. I would also like to thank the rest members of my defense committee: Prof. Joshua J. Choi, Prof. Israel Klich, Prof. Gia-Wei Chern, for their comments, suggestions, and questions which help improve my research from various perspectives.

Next, I thank Dr. Daniel M. Pajerowski, Dr. Douglas L. Abernathy, Dr. Ryoichi Kajimoto, Dr. Mitsutaka Nakamura, Dr. Qiang Zhang, Dr. Craig M. Brown, and Dr. Guangyong Xu for their help in neutron scattering experiments. I also give my thanks to Dr. Wei-Liang Chen and Prof. Yu-Ming Chang for their tremendous effort in the photoluminescence measurements. I would like to thank Dr. Mina Yoon for her help in the density functional theory calculations. I also thank Mr. Eric N. Holmgren, Mr. Qing Huang, and Prof. Haidong Zhou for providing the high-quality samples for my experiments.

My deep gratitude also goes to my fellow lab-mates, Dr. Tianran Chen, Dr. Depei Zhang, and Ms. Haritha Sindhu Rajeev, for the days we were working together and for all the fun we shared. I am especially grateful to Dr. Depei Zhang, who taught me details of experimental and calculation techniques. Furthermore, I thank my parents and all my friends for their supports and encouragements during my Ph. D. period.

Finally, I acknowledge the funding sources in my research. The work at the University of Virginia was supported by the U.S. Department of Energy, Office of

Science, Office of Basic Energy Sciences under Award Number DE-SC0016144. The research at Oak Ridge National Laboratory's Spallation Neutron Source was sponsored by the U.S. Department of Energy, Office of Basic Energy Sciences. We acknowledge the support of the Material and Life Science Experimental Facility, Japan Proton Accelerator Research Complex, in providing the neutron research facilities used in this work. The work at National Taiwan University was supported by the Center of Atomic Initiative for New Materials (AI-MAT) from the Featured Areas Research Center Program within the framework of the Higher Education Sprout Project by the Ministry of Education in Taiwan (108L9008). Additional supports were provided by the Ministry of Science and Technology of Taiwan (Grant No. MOST 105-2119-M-002-046-MY3 and MOST 107-2112-M-002-024-MY3). The computational work was performed by utilizing the resources at the National Energy Research Scientific Computing (NERSC) Center, which is supported by the Office of Science of the U.S. Department of Energy (Contract No. DE-AC02-05CH11231).

Table of Contents

Author's Biographical Sketch.....	v
Acknowledgments.....	vi
List of Figures.....	x
List of Tables.....	xii
Chapter 1. Introduction.....	1
1.1 Strongly Correlated Systems.....	2
1.2 Weakly Correlated Systems.....	5
1.3 Neutron Scattering.....	7
Chapter 2. Spin correlations in $\text{Sr}_2\text{CuTe}_{0.5}\text{W}_{0.5}\text{O}_6$	17
2.1 Magnetic Excitation Spectra.....	23
2.2 Spatial Correlations.....	29
2.3 Dynamic Susceptibility.....	31
2.4 Spin Jam State.....	34
Chapter 3. $(\text{BA})_2\text{PbI}_4$ & $(\text{PEA})_2\text{PbI}_4$: Structural Dynamics and Optoelectronic Properties	36
3.1 Experimental Techniques.....	36
3.1.1 Sample preparation.....	36
3.1.2 Neutron Scattering Measurements.....	37
3.2 Theoretical Analysis and Calculations.....	38
3.2.1 Density Functional Theory Calculations.....	38

3.2.2 Rotational Mode Calculations.....	39
3.3 Structural Dynamics and Optoelectronic Properties.....	41
3.3.1 Vibrational Dynamics.....	41
3.3.2 Rotational Dynamics.....	48
3.3.3 Connections with Optoelectronic Properties	53
Chapter 4. Summary	58
Appendix 1. Magnetic Scattering Experimental Details.....	60
Appendix 2. Normalization to Elastic Incoherent Scattering Intensity	70
Appendix 3. Jump Model Details	71
Appendix 4. Rotational Contribution Estimation	77
References.....	79

List of Figures

Figure 1. Schematic of geometrical frustrations	3
Figure 2. Quantum spin liquid candidates	5
Figure 3. Schematic of crystal structures of double perovskites $\text{Sr}_2\text{CuTe}_{1-x}\text{W}_x\text{O}_6$	17
Figure 4. Magnetic structure and orbital configurations of $\text{Sr}_2\text{CuTeO}_6$	18
Figure 5. Magnetic structure and orbital configurations of Sr_2CuWO_6	19
Figure 6. Magnetic excitations of $\text{Sr}_2\text{CuTeO}_6$ and Sr_2CuWO_6	20
Figure 7. Schematic phase diagram of $\text{Sr}_2\text{CuTe}_{1-x}\text{W}_x\text{O}_6$	21
Figure 8. Inelastic neutron scattering data of $\text{Sr}_2\text{CuTe}_{0.5}\text{W}_{0.5}\text{O}_6$	24
Figure 9. Low energy spin fluctuations of $\text{Sr}_2\text{CuTe}_{0.5}\text{W}_{0.5}\text{O}_6$	26
Figure 10. Low energy spin fluctuations and spectral weight of $\text{Sr}_2\text{CuTe}_{0.5}\text{W}_{0.5}\text{O}_6$	27
Figure 11. The elastic magnetic scattering cross section of $\text{Sr}_2\text{CuTe}_{0.5}\text{W}_{0.5}\text{O}_6$	28
Figure 12. Q -dependence of low energy spin fluctuations in $\text{Sr}_2\text{CuTe}_{0.5}\text{W}_{0.5}\text{O}_6$	30
Figure 13. $\hbar\omega$ -dependence of low energy spin fluctuations in $\text{Sr}_2\text{CuTe}_{0.5}\text{W}_{0.5}\text{O}_6$	32
Figure 14. Spin correlation length and relaxation rate of the low energy spin fluctuations in $\text{Sr}_2\text{CuTe}_{0.5}\text{W}_{0.5}\text{O}_6$	33
Figure 15. Schematic of crystal structure of $(\text{BA})_2\text{PbI}_4$ and $(\text{PEA})_2\text{PbI}_4$	43
Figure 16. Experimental phonon spectra and DFT calculations of $(\text{BA})_2\text{PbI}_4$	45
Figure 17. Experimental phonon spectra and DFT calculations of $(\text{PEA})_2\text{PbI}_4$	46
Figure 18. Statistics of number of phonon modes with different Pb-I vibrational energy fractions for $(\text{BA})_2\text{PbI}_4$ and $(\text{PEA})_2\text{PbI}_4$	47

Figure 19. Temperature-dependent quasi-elastic neutron scattering spectra of $(\text{BA})_2\text{PbI}_4$ and $(\text{PEA})_2\text{PbI}_4$ upon heating.....	49
Figure 20. Visualization of rotational modes in $(\text{BA})_2\text{PbI}_4$ and $(\text{PEA})_2\text{PbI}_4$	50
Figure 21. Constant energy slices of QENS spectra and fittings of $(\text{BA})_2\text{PbI}_4$	51
Figure 22. Constant energy slices of QENS spectra and fittings of $(\text{PEA})_2\text{PbI}_4$	52
Figure 23. Q -integrated phonon spectra of $(\text{BA})_2\text{PbI}_4$ and $(\text{PEA})_2\text{PbI}_4$ as a function of temperature	54
Figure 24. Temperature-dependent phonon intensities, rotational contributions and PLQY of 2D MHPs.....	55
Figure 25. Phenomenological $S(Q)$ fittings of low-energy spin fluctuations of $\text{Sr}_2\text{CuTe}_{0.5}\text{W}_{0.5}\text{O}_6$	68
Figure 26. Rotational modes of organic molecules in $(\text{BA})_2\text{PbI}_4$ and equivalent H sites for NH_3 , CH_3 , and CH_2 groups	73
Figure 27. Temperature dependent elastic channel data in rotational contribution estimation.....	77

List of Tables

Table S1. Character tables for C_3 and C_4	71
Table S2. Model details for jump mode $\Gamma = C_4 \otimes C_3$	72
Table S3. Model details for jump mode $\Gamma = C_4$	73
Table S4. Structure factors for jump mode $\Gamma = C_3$	74
Table S5. Relaxation times τ_{C_4} and τ_{C_3} for the rotations of organic molecules in (BA) ₂ PbI ₄ and (PEA) ₂ PbI ₄	75
Table S6. Estimated relaxation times and the mean squared displacement for the rotations of organic molecules in (BA) ₂ PbI ₄ and (PEA) ₂ PbI ₄	78

Chapter 1

Introduction

The field of correlated electron systems has been one of the most widely studied areas of research in condensed-matter physics. These compounds are typically made of simple blocks, such as a transition-metal ion centered in an octahedral of oxygen or halide cage forming a perovskite structure. The ensemble of these elements behaves in a complex manner leading to remarkable properties, such as metal-insulator transition and high- T_c superconductivity [1, 2]. Due to the non-negligible Coulomb interactions between electrons in these systems, the collective states cannot be understood via one-electron approximation that one electron is embedded in a static mean field generated by other electrons. The interplay of interacting or ‘correlated’ electrons’ internal degrees of freedom, i.e. spin moment and charge, can exhibit a pool of non-trivial ordering phenomena. This interplay makes correlated electron systems quite sensitive to the external environment, such as magnetic field, temperature, pressure, or doping [3].

To theoretically describe correlated electron systems, the Hubbard model [4] was proposed in 1963. The Hubbard model is based on the tight-binding approximation from condensed-matter physics, which describes particles in a periodic potential. The Hamiltonian is written in terms of Wannier states, which are localized states centered on each lattice site. Wannier states on neighboring sites are coupled, allowing particles on one site to ‘hop’ to another. Mathematically, the Hamiltonian is made up of two terms. The first term describes the kinetic energy of the system, parameterized by the so-called

hopping integral t . The second term is the on-site interaction of strength U . Written out in second quantization form for a simple 1D correlated electron system, the Hubbard Hamiltonian takes the format [5]

$$\hat{H} = - \sum_{i,j,\sigma,\sigma'} t_{ij} (\hat{c}_{i,\sigma}^+ \hat{c}_{j,\sigma'} + \hat{c}_{j,\sigma'}^+ \hat{c}_{i,\sigma}) + U \sum_i \hat{n}_{i\uparrow} \hat{n}_{i\downarrow} \quad (\text{Eq. 1})$$

where $\hat{n}_{i,\sigma} = \hat{c}_{i,\sigma}^+ \hat{c}_{i,\sigma}$ is the spin-density operator for spin σ on the i -th site. According to the ratio of the hopping integral and interaction strength t/U , correlated electron systems can be generally categorized into two types: strongly correlated and weakly correlated systems. In the limit of $t/U \gg 1$, the electron-electron interaction can be ignored, leaving the system equivalent to free electron gas, which is an extreme case for weakly correlated systems. On the other hand, a strongly correlated electron system can be described by a much larger Coulomb repulsion among electrons ($U \gg t$).

1.1 Strongly correlated systems

For strongly correlated systems, one of the emergent phenomena is the frustrated magnetism [6]. The term ‘frustrated’ describes systems where competing interactions cannot be satisfied simultaneously or dominant interactions are randomly distributed due to sophisticated behaviors of lattice ions and interacting electrons.

The studies of magnetic frustration began with the simplest antiferromagnets, a two-dimensional (2D) triangular lattice of Ising spins (of which the orientations are in

one of two states along one direction, i.e. ‘up’ or ‘down’). In 1950, Wannier showed that this system has a large degeneracy of ground states [7]. As shown in Fig. 1(A), with only antiferromagnetic (AF) nearest-neighbor interactions, the spins of the triangular lattice are frustrated due to its intrinsic symmetry. This is called ‘geometric frustration’, which is a prototype of magnetic frustration.

Another commonly seen competing-interaction example is the square lattice with

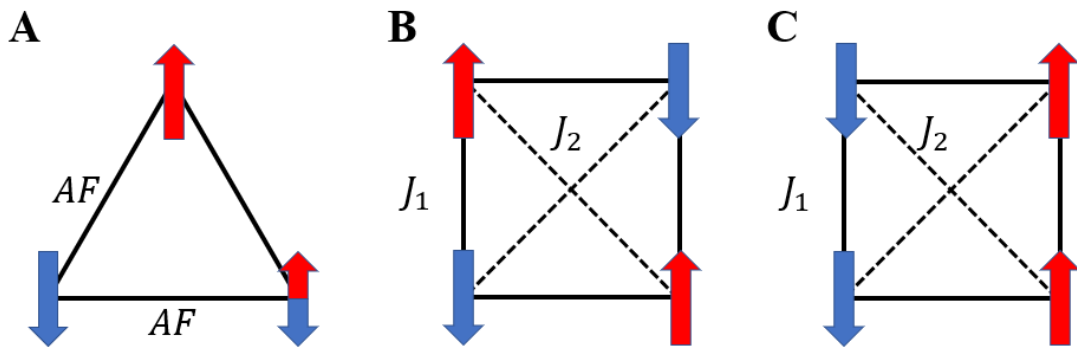


Fig. 1 Schematic of geometrical frustrations.

(A) *Triangular Ising spin lattice. Red arrows represent spin pointing up and blue arrows represent spin pointing down. ‘AF’ represents antiferromagnetic interactions.*
 (B)(C) *Square-lattice J_1 - J_2 models, showing ground state spin configurations with $J_1 \gg J_2$ (B) and $J_1 \ll J_2$ (C).*

competing nearest-neighbor (J_1) and next-nearest-neighbor (J_2) interactions (Fig. 1 (B)(C)). The ground state of this model highly depends on the ratio of the interactions J_1/J_2 . For $J_1 \gg J_2$, the nearest neighbor spins are antiparallel, enforcing the parallel (ferromagnetic) alignments of next-nearest-neighbor spins. When $J_1 \ll J_2$, the next-nearest-neighbor spins are antiferromagnetically aligned. Things would get quite

complicated when J_1 is comparable with J_2 where the system is expected to have the highest degeneracy and strongest frustration.

Following this square lattice model, another type of frustrated magnets attracted extensive interests, called the interaction disordered magnets [8-12], where the system exhibits a random distribution of spin interactions instead of the ordered competing interactions. The interaction disorder in this type of magnets could be due to several reasons, such as site-disorder of the magnetic ions, random distribution of non-magnetic ions and doping of several types of non-magnetic ions.

The disordered interactions could give rise to a large degeneracy of the ground state. Under particular circumstances, it can lead to an exotic state of matter, spin liquids, in which the spins are highly entangled and stay fluctuating well below its Curie-Weiss temperature at which the specific magnetic interactions in the material become paramagnetic upon heating. In a spin liquid, the frustration of spins can be characterized as classical and quantum. Classical frustrations predominate for large spins (spin S much larger than the minimum $1/2$) while quantum fluctuations play a prominent role in small spin systems where spin S is comparable to $1/2$. Strong quantum fluctuations result in a quantum spin liquid (QSL) where spins are highly entangled and pointing in random orientations [13]. As an extraordinary example of magnetic frustration, the concept of quantum spin liquid originates from Anderson's 1973 paper [14] which describes an antiferromagnetic spin- $1/2$ triangular lattice exhibiting strong zero-fluctuations that prevent conventional magnetic long-range order. In 1987, QSL experienced an explosion of interest when it was related to high-temperature cuprate superconductors [15], the fractional quantum hall effect [16], and topological order [17-19]. Since then, extensive

work has been done in searching for QSL candidates in nature. Some QSL candidates are listed in Fig. 2.

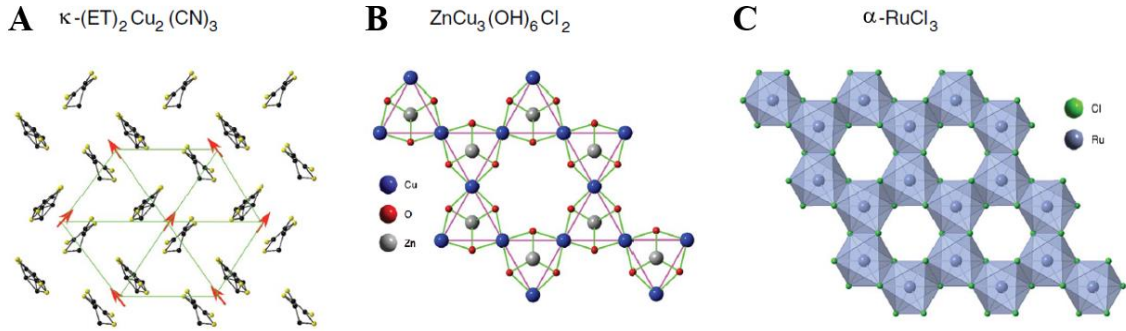


Fig. 2 Quantum spin liquid candidates.

(A) $\kappa\text{-(ET)}_2\text{Cu}_2(\text{CN})_3$, where *ET* is bis(ethylenedithio)tetrathiafulvalene Ref. [20-23].
(B) herbertsmithite [23-27]. (C) $\alpha\text{-RuCl}_3$ [23,28,29]. The figure is obtained from Ref. [23].

1.2 Weakly correlated systems

In weakly correlated electron systems, electrons experience relatively weaker Coulomb repulsion from other electrons and behaviors of single electron become easier to understand. As one of the centerpieces of weakly correlated electron systems, the class of optoelectronic materials has attracted extensive attention due to its ability of transferring energy in the forms of light or electricity, such as solar cells and light emitting devices.

Among the large number of optoelectronic materials, a special class of perovskites, called the hybrid organic-inorganic perovskites (HOIPs), has come to the forefront of the optoelectronic research field. Working as solar cells, three-dimensional (3D) HOIPs, for example MAPbI₃ (methylammonium lead iodide), make themselves advantageous with their high defect tolerance [30, 31], comparable power conversion efficiency ~25% [32] to conventional silicon-based solar cells, and surprisingly low fabrication costs. As for the conventional silicon-based cells, extremely high temperature (over 2000 K) that is needed in the manufacturing of silicon wafers and a large amount of chemical waste that follow make it quite expensive. On the other hand, HOIPs are much cheaper: dissolving the two halide salts AX and BX₂ in an organic solvent and evaporating the solution at relatively low temperatures, usually below 400 K, will form the perovskite crystals.

Another important application of HOIPs, especially for the low-dimensional HOIPs, is the light-emission diodes (LEDs). In the LED field, the most important factors are photoluminescence quantum yield (PLQY) and full-width-at-half-maximum (FWHM) of the emitted spectrum. Two-dimensional (2D) HOIPs possess self-assembled layered structures which induce dielectric- and quantum-confinement effects [33-38]. The strong confinements subsequently cause the formation of excitons with large binding energy (usually a few hundred meVs). Here, exciton is a quasi-particle formed by two oppositely charged carriers, i.e., an electron and a hole. Thus, during photo-excitation, large numbers of stable excitons will accumulate in the recombination centers which significantly improves the recombination efficiency and leads to high PLQY [33, 37, 38]. For example, Gong et al. [37] demonstrated that the 2D exfoliated single crystal,

(PEA)₂PbBr₄, can exhibit a maximum PLQY of 79 % along with a much narrower emission linewidth (FWHM of 20 nm compared with 75 nm for organic emitters).

1.3 Neutron scattering

As mentioned above, correlated electron systems exhibit numerous exotic properties. Then the questions arise: How can we explore the microscopic mechanism behind them? How can we ‘observe’ the behaviors of atoms, spins, or charge carriers in these systems? To do that, we need a tool whose characteristic scale (etc. wavelength) is not larger than that of the microscopic object (typical atomic spacing is 2 Å in a solid). X-rays, particle beams of electrons, neutron, and light atom scatterers can all have wavelength or de Broglie wavelengths of 1~10 Å. Neutrons make themselves extraordinary because they have no electric charge and hence can penetrate far deeper into solids than others. The neutron also has a magnetic moment which makes it the most effective way to directly probe the spatial and time-dependent spin correlations in magnetic systems via dipole-dipole interactions.

In the neutron scattering process, the total energy and momentum are conserved. The momentum transfer from the neutron to the sample is defined as $Q = k - k'$ where k and k' are the wave vector of the incident and scattered neutron, respectively. The amount of energy the sample gained from neutron is $\hbar\omega = \frac{\hbar^2}{2m}(k^2 - k'^2)$ where m is the mass of the neutron. There are two types of scattering between neutrons and materials: nuclear scattering and magnetic scattering. The intensity of nuclear scattering is proportional to the spatial correlation function of nuclei [39]

$$\frac{\partial^2 \sigma}{\partial \Omega \partial \omega} = \frac{k'}{k} \frac{1}{2\pi\hbar} \sum_{jj'} \overline{b_j b_{j'}} \int_{-\infty}^{\infty} \langle \exp(-i\mathbf{Q} \cdot \mathbf{R}_j(0)) \exp(i\mathbf{Q} \cdot \mathbf{R}_{j'}(t)) \rangle \exp(-i\omega t) dt$$

(Eq. 2)

where b_j is the scattering length for the nuclei j .

The intensity of magnetic scattering is proportional to the spin-spin correlation function [39]

$$\begin{aligned} \frac{\partial^2 \sigma}{\partial \Omega \partial \omega} &= \frac{(\gamma r_0)^2 k'}{2\pi\hbar} \frac{k'}{k} N \left| \frac{1}{2} g f(\mathbf{Q}) \right|^2 \sum_{\alpha\beta} (\delta_{\alpha\beta} - \widehat{Q}_\alpha \widehat{Q}_\beta) \sum_l \exp(i\mathbf{Q} \cdot \mathbf{l}) \\ &\quad \times \int_{-\infty}^{\infty} \langle \exp(-i\mathbf{Q} \cdot \mathbf{u}_0(0)) \exp(i\mathbf{Q} \cdot \mathbf{u}_l(t)) \rangle \\ &\quad \times \langle S_0^\alpha(0) S_l^\beta(t) \rangle \exp(-i\omega t) dt \end{aligned}$$

(Eq. 3)

where $\mathbf{u} = \mathbf{R} - \mathbf{l}$, $g \approx 2$, $f(\mathbf{Q})$ is the magnetic form factor, $\frac{\gamma r_0}{2} = 0.2695 \times 10^{-12}$ cm, α, β denote the Cartesian Coordinates x, y , and z , and $\widehat{Q}_\alpha, \widehat{Q}_\beta$ are the projections of the unit wave-vector $\widehat{\mathbf{Q}}$ on the Cartesian axes.

The nuclear scattering is widely used in crystal structure determination, rotational dynamics of organic molecules, and lattice vibrational dynamics. In real experimental data, the nuclear scattering intensity consists of two parts: coherent scattering and incoherent scattering. Assuming there is no correlation between the values of b for any two nuclei

$$\overline{b_j b_{j'}} = (\bar{b})^2, \quad j' \neq j$$

$$\overline{b_j b_{j'}} = \bar{b}^2, \quad j' = j$$

Then we have

$$\begin{aligned} \frac{\partial^2 \sigma}{\partial \Omega \partial \omega} &= \frac{k'}{k} \frac{1}{2\pi\hbar} (\bar{b})^2 \sum_{jj'} \int \langle j', j \rangle \exp(-i\omega t) dt \\ &+ \frac{k'}{k} \frac{1}{2\pi\hbar} \{ \bar{b}^2 - (\bar{b})^2 \} \sum_j \int \langle j, j \rangle \exp(-i\omega t) dt \end{aligned} \quad (\text{Eq. 4})$$

where $\langle j', j \rangle = \langle \exp(-i\mathbf{Q} \cdot \mathbf{R}_j(0)) \exp(i\mathbf{Q} \cdot \mathbf{R}_{j'}(t)) \rangle$.

The first term is known as coherent scattering cross-section. It depends on the correlation between the positions of different nuclei and the same nucleus at different times, thus it describes the nuclear interference. The second term is called incoherent scattering which only contains the correlation between the positions of the same nucleus at different time.

In crystal structure determination, elastic coherent scattering is manifested as sharp Bragg peaks.

$$\left(\frac{d\sigma}{d\Omega} \right)_{coh,el} = \frac{N(2\pi)^3}{v_0} \sum_{\boldsymbol{\tau}} \delta(\mathbf{Q} - \boldsymbol{\tau}) |F_N(\mathbf{Q})|^2 \quad (\text{Eq. 5})$$

where v_0 is the unit cell volume, $\boldsymbol{\tau}$ is the reciprocal lattice vector for certain nuclear Bragg peak. $F_N(\mathbf{Q}) = \sum_d \bar{b}_d \exp(i\mathbf{Q} \cdot \mathbf{d}) \exp(-W)$ is known as the nuclear structure

factor, where \mathbf{d} is the position of certain atom in the unit cell and $\exp(-W)$ is related to averaged atomic displacements, $W = \langle (\mathbf{Q} \cdot \mathbf{u})^2 \rangle$. By fitting the calculations to experimental scattering data, people can obtain the microscopic structural information of the target material.

As for the investigations of dynamics, quasi-elastic and inelastic neutron scattering help us characterize slow dynamics and collective vibrations, respectively. Slow dynamics include diffusion, molecule rotations, and atomic relaxation processes. A slow dynamic process with relaxation time τ , which is then proportional to $\exp(-t/\tau)$, will be manifested as Lorentzian profile centered at the elastic channel ($\hbar\omega = 0$) after Fourier transformation from time domain to energy domain. Quasi-elastic scattering focuses on the region of small energy transfers with atoms of the sample, typically ± 2 meV. These energy transfers originate from the interactions between neutrons and diffusing atoms or reorienting molecules over a time scale of 1~100 picoseconds [40]. Different methods can be used to analyze the experimental quasi-elastic data, such as phenomenological Lorentzian profile fitting to the momentum (Q)-integrated spectra, $S(\hbar\omega)$, and more detailed modeling to $S(Q, \hbar\omega)$ along with group theory analysis. Note that when we analyze the relaxation process in the sample, we refer to the behaviors of the same atom at different times. Thus, we will focus on analyzing the incoherent scattering intensity of the materials.

As for the collective vibrations, the energy and momentum conservation are transformed as

$$\frac{\hbar^2}{2m}(k^2 - k'^2) = \hbar\omega_s, \quad \mathbf{Q} = \mathbf{k} - \mathbf{k}' = \boldsymbol{\tau} + \mathbf{q}$$

where \mathbf{q} is the wavevector of certain vibrational normal mode s . This is called one-phonon coherent scattering. To identify phonon modes from experimental spectra properly, we can perform density-functional-theory (DFT) calculations to solve the equation of vibrational motion in 3D space numerically. It outputs the vibrational energies and eigenvectors of different phonon modes so that we can characterize them via vibrational energy fractions of different atoms and visualize the detailed atomic motions. This helps us get a better view of the microscopic atomic world.

In addition to the nuclear scattering, the magnetic scattering also plays a significant role in exploring the microscopic condensed-matter world. As we said previously, the magnetic neutron scattering intensity comes from the interactions of neutrons' magnetic moments with dipoles formed by unpaired electrons in the sample. Thus, it can offer us valuable information about the magnetic system, such as the magnetic spin order and spin excitations (etc. spin wave, magneto-vibrations). One of the most important applications of magnetic neutron scattering is magnetic neutron diffraction. It is used to determine the spatial distribution and orientations of the atomic magnetic moments in the magnetically ordered systems as a function of external parameters, such as temperature, pressure, or magnetic field. If someone would like to evaluate the magnetic excitations or fluctuations of the sample, inelastic magnetic neutron scattering helps a lot. It is the only technique that can directly probe the entire magnetic excitation spectrum. As a result, researchers prefer performing external-parameter-dependent inelastic magnetic scattering measurements to study possible critical behaviors of spin correlations in the sample.

For a powder sample, the magnetic neutron scattering probes the spherically averaged scattering function

$$S(Q, \hbar\omega) = \int \frac{d\Omega}{4\pi} \frac{1}{2} \sum_{\alpha\beta} (\delta_{\alpha\beta} - \widehat{Q}_\alpha \widehat{Q}_\beta) S^{\alpha\beta}(\mathbf{Q}, \hbar\omega)$$

(Eq. 6)

where

$$S^{\alpha\beta}(\mathbf{Q}, \hbar\omega) = \frac{1}{2\pi\hbar} \sum_l \exp(i\mathbf{Q} \cdot \mathbf{l}) \int_{-\infty}^{\infty} \langle S_0^\alpha(0) S_l^\beta(t) \rangle \exp(-i\omega t) dt$$

(Eq. 7)

One has to be very careful that the measured intensity consists of various sources: background (in time-of-flight spectroscopy it is called ‘time-constant background’), neutron scattering from instrument or equipment (such as sample chamber), (nuclear and magnetic) scattering from the sample. The scattering from the sample is characterized as useful experimental data. To filter out the useful data, ‘empty-sample-can’ scans are usually performed. By directly subtracting the ‘empty-sample-can’ data from the raw data, one can get the effective data from the sample. Another method to get rid of the background signal in the raw data, under the circumstance that the ‘empty-sample-can’ scans are not performed, is to process the data based on the detailed balance condition [39], $S(-\omega, T) = e^{-\frac{\hbar\omega}{k_B T}} S(\omega, T)$.

First, we denote the raw intensity on the energy-lose side from a certain Q -cut, $(Q, Q + \Delta Q)$, as

$$I(\omega, T) = bkg(\omega) + S(\omega, T)$$

(Eq. 8)

where $bkg(\omega)$ represents the background signal which does not satisfy the detailed balance condition. It contains the background counting, scattering from equipment, and nuclear and magnetic elastic scattering. $S(\omega, T)$ represents the scattering intensity which satisfies the detailed balance condition, including inelastic magnetic excitations and nuclear scattering (phonons). The quasi-elastic signal that diffuses beyond the elastic resolution channel is also included. For the energy-gain side, by applying the detailed balance condition, the intensity is written as

$$I(-\omega, T) = bkg(-\omega) + S(\omega, T)e^{-\frac{\hbar\omega}{k_B T}}$$

(Eq. 9)

Assuming the background signal $bkg(\pm\omega)$ is temperature-independent, with full energy range ($\pm\hbar\omega$) data at multiple temperatures, we can extract the optimized $S(\omega, T)$ for certain $\hbar\omega$ by minimizing the deviation

$$Dev = \sum_T \frac{[I(\omega, T) - bkg(\omega) - S(\omega, T)]^2}{\sigma^2(\omega, T)} + \frac{[I(-\omega, T) - bkg(-\omega) - S(\omega, T)e^{-\hbar\omega/k_B T}]^2}{\sigma^2(-\omega, T)}$$

(Eq. 10)

where σ is the error of the experimental data. To minimize the deviation, we take derivatives of Dev with respect to unknown parameters (see details in Appendix 1).

Another key point in magnetic neutron scattering data processing is the physical meaning of the intensity unit. The measured raw intensity is usually in a relative scaling, which is commonly called ‘arbitrary unit’. Sometimes obtaining only this relative intensity is sufficient. However, in order to better study the spin dynamics such as frozen spin moments, it is necessary to convert the relative magnetic scattering intensity into absolute units, such as in terms of magnetic moment μ_B or spin S . To transform the intensity into the absolute unit, one could use following references [41]: (1) nuclear Bragg peak intensity; (2) sample incoherent elastic scattering; (3) standard sample (such as vanadium) incoherent elastic scattering, and (4) sample phonon scattering. In our work for the strongly correlated system, we rescale the raw data into the absolute unit with respect to the nuclear Bragg peak intensity. To check the validity of the absolute unit normalization, one could refer to the sum rule (see details in Appendix 1)

$$\frac{\int_{-\infty}^{\infty} \int_{BZ} \tilde{S}(Q, \omega) dQ d\omega}{\int_{BZ} dQ} = \frac{2}{3} S(S + 1) \delta_{\alpha\beta}$$

(Eq. 11)

where $\tilde{S}(Q, \omega)$ is the rescaled intensity.

In this thesis, we reported our neutron scattering studies on a strongly correlated magnetic system, $\text{Sr}_2\text{CuTe}_{0.5}\text{W}_{0.5}\text{O}_6$, and two weakly correlated non-magnetic systems, $(\text{BA})_2\text{PbI}_4$ (butylammonium lead iodide) and $(\text{PEA})_2\text{PbI}_4$ (phenethyl-ammonium lead iodide).

For $\text{Sr}_2\text{CuTe}_{0.5}\text{W}_{0.5}\text{O}_6$, a square-lattice magnet with super-exchange between $S = 1/2$ Cu^{2+} spins mediated by randomly distributed Te and W ions, by using sub-K temperature and 20 μeV energy resolution neutron scattering experiments, we show that the system below $T_f = 1.7(1)$ K exhibits an extremely weak frozen moment of $\langle S \rangle / S \sim 0.1$. Below T_f the imaginary part of the dynamical susceptibility, $\chi''(\hbar\omega)$, behaves linearly with $\hbar\omega$ for $\hbar\omega < k_B T_f$ where k_B is the Boltzmann constant with the characteristic spin relaxation rate increasing with decreasing temperatures. Above T_f , $\chi''(\hbar\omega)$ behaves as $\tan^{-1}(\hbar\omega/\Gamma_{min})$ at low energies indicating the presence of a distribution of the spin relaxation rate with the lower limit Γ_{min} , which behaves as a power law with temperature, $\Gamma_{min}/|J| = \left(\frac{k_B T}{|J|}\right)^\alpha$, with $|J| \sim 9$ meV and $\alpha = 1.3(1)$. On the other hand, the spatial spin correlations are two-dimensional and short-range with an in-plane correlation length of $\xi \sim \sqrt{2} d_{NN}$, where d_{NN} is the distance between the nearest-neighbor spins. Our results indicate that $\text{Sr}_2\text{CuTe}_{0.5}\text{W}_{0.5}\text{O}_6$ transits from a gapless disorder-induced spin liquid to a new quantum state below T_f , exhibiting a weak frozen moment and low energy dynamic susceptibility that is linear in energy consistent with a Halperin-Saslow-like excitation which is surprising for such a weak freezing in this highly fluctuating quantum regime.

For $(\text{BA})_2\text{PbI}_4$ and $(\text{PEA})_2\text{PbI}_4$, we attempted to link their crystal structural dynamics, such as molecular rotational dynamics and lattice vibrational dynamics, to their temperature-dependent photoluminescence quantum yield (PLQY) indicated by their bromide equivalents. By performing temperature-dependent quasi-elastic neutron scattering measurements and applying group theory analysis, we identified the rotational

modes of BA^+ cation and PEA^+ cation. The neutron scattering measurements and data analysis revealed two types of jump rotational modes for BA^+ cation: the four-fold (C_4) modes of the entire cation about the crystallographic c -axis, which only gets activated in the high-temperature phase ($T > 275 \text{ K}$); the three-fold (C_3) mode of NH_3 and CH_3 terminal groups about their own symmetry axis throughout the temperature range. On the other hand, we proposed that within the interested temperature range in this study (7~300 K), the PEA^+ cation only possesses the C_3 mode of its NH_3 group. Furthermore, with wide energy-range temperature-dependent inelastic neutron scattering measurements ($E_i = 10, 30, 62, 115, 250, 712 \text{ meV}$) and density-functional-theory (DFT) calculations, we evaluated phonon spectra for both samples and characterized their phonons into three types, i. e. inorganic modes, hybrid modes, and organic modes based on their vibrational energy fractions.

We examined the correlations between the device performance (PLQY) and structural dynamics for both samples by comparing their temperature dependence. The molecular rotational dynamics of the two samples are found to show an excellent correspondence to the PLQY indicated by their equivalents that we assume to be similar with or same as the iodides. We argue that the rotational motion of the charged molecules plays a more crucial role than the lattice vibrations in the optoelectronic properties of these 2D MHPs.

Chapter 2

Spin correlations in $\text{Sr}_2\text{CuTe}_{0.5}\text{W}_{0.5}\text{O}_6$

Recently, as an idealistic realization of the $S = 1/2$ square-lattice $J_1 - J_2$ model, the double perovskite compound, $\text{Sr}_2\text{CuTe}_{1-x}\text{W}_x\text{O}_6$ has obtained revival interest due to its significant magnetic frustration away from its clean limit ($x = 0$ and 1), which further suggests that it could be an excellent spin liquid candidate. The crystal structure is shown in Fig. 3. It was reported that the difference of d orbital hybridizations of Te ($4d^{10}$) and W ($5d^0$) ions leads to dramatic changes in exchange interactions [42].

Let's first look at the two parent compounds, $x = 0$ and $x = 1$. For $\text{Sr}_2\text{CuTeO}_6$ ($x = 0$), the previous neutron diffraction measurement [43] showed the Neel

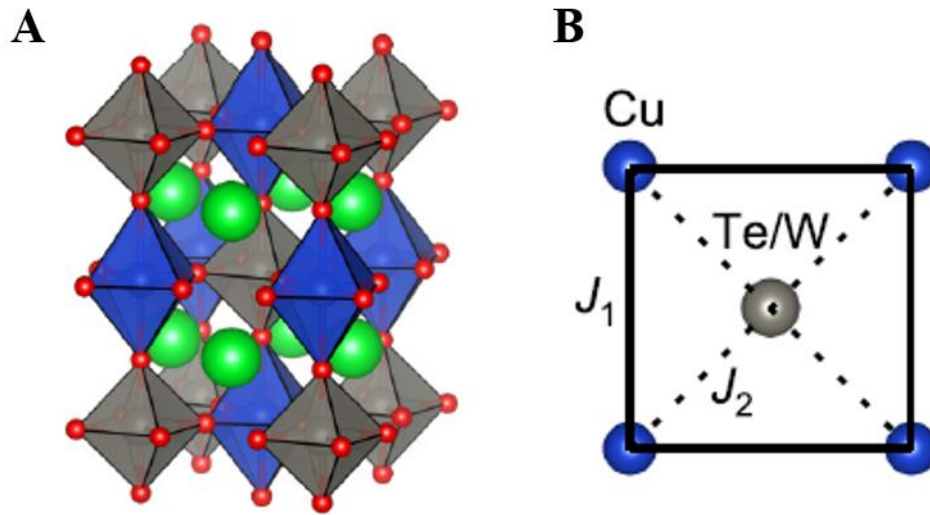


Fig. 3 Schematic of crystal structures of double perovskites $\text{Sr}_2\text{CuTe}_{1-x}\text{W}_x\text{O}_6$.

(A) The B-site ordered double-perovskite crystal structure. (B) The square lattice formed by $S = 1/2$ Cu^{2+} ions with the view down the c -axis. The Te or W cation in the center determines the J_1 and J_2 interactions. The figure is extracted from Ref. [44].

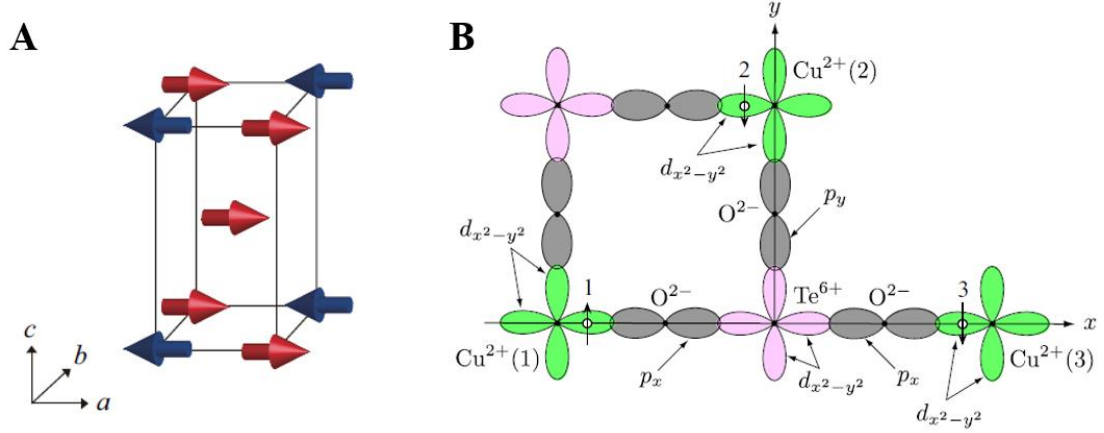


Fig. 4 Magnetic structure and orbital configurations of Sr₂CuTeO₆.

(A) The Neel order magnetic structure with a wave vector $q_m = (1/2, 1/2, 0)$. (B) The electron orbital configurations related to Cu²⁺ - O²⁻ - Te⁶⁺ - O²⁻ - Cu²⁺. The figure is extracted from Ref. [43].

antiferromagnetic ordering where the nearest-neighbor spins are antiparallely aligned in *ab* plane (Fig. 4 (A)), characterized by a propagation vector $q_m = \left(\frac{1}{2}, \frac{1}{2}, 0\right)$. The temperature-dependent measurements of the magnetic Bragg peak intensity showed the Neel temperature to be ~ 29 K. To evaluate the origin of the dominating nearest-neighbor (J_1) interactions, Koga *et al.* [43] started from the electron orbitals (Fig. 4 (B)) [42, 43]. They argued that the p_x and p_y orbitals of O²⁻ will have strong overlaps with $d_{x^2-y^2}$ orbital of Te⁶⁺ ions and they form a molecular orbital. The $d_{x^2-y^2}$ orbitals of Cu²⁺(1) and Cu²⁺(2) share the same molecular orbital in which case the two spins on them have to be antiparallel according to Pauli principle. This orbital coupling leads to antiferromagnetic interaction between Cu²⁺(1) and Cu²⁺(2) (J_1). Similar analysis applies to that between Cu²⁺(1) and Cu²⁺(3) (J_2). However, there are two paths for J_1 but only one for J_2 and each

path makes almost the same contributions. Therefore, it can be expected J_1 will dominate in $\text{Sr}_2\text{CuTeO}_6$.

For Sr_2CuWO_6 ($x = 1$), another type of magnetic ordering, columnar antiferromagnetic ordering, was found below its Neel temperature ~ 24 K with a characteristic wave vector $\mathbf{q}_m = \left(0, \frac{1}{2}, \frac{1}{2}\right)$ [45] (Fig. 5 (A)). In this case [42, 43], Koga *et al.* claimed that the W ion ($5d^0$) makes significant differences to the orbital configurations. The $5p$ orbitals (p_x, p_y) of W^{6+} ions overlap strongly with the p orbitals of O^{2-} (Fig. 5 (B)). The $p_x - p_x$ and $p_y - p_y$ pairs form two different orthogonal molecular orbitals. The $d_{x^2-y^2}$ orbitals of $\text{Cu}^{2+}(1)$ and $\text{Cu}^{2+}(2)$ couple to different molecular orbitals in which case their spins will align parallelly due to Hund's rule. As a result, the $\text{Cu}^{2+}(1) - \text{Cu}^{2+}(2)$ interaction will be ferromagnetic. Yet, for interaction between $\text{Cu}^{2+}(1)$ and $\text{Cu}^{2+}(3)$, they both couple to the same $p_x - p_x$ molecule orbital, so their spins have to be

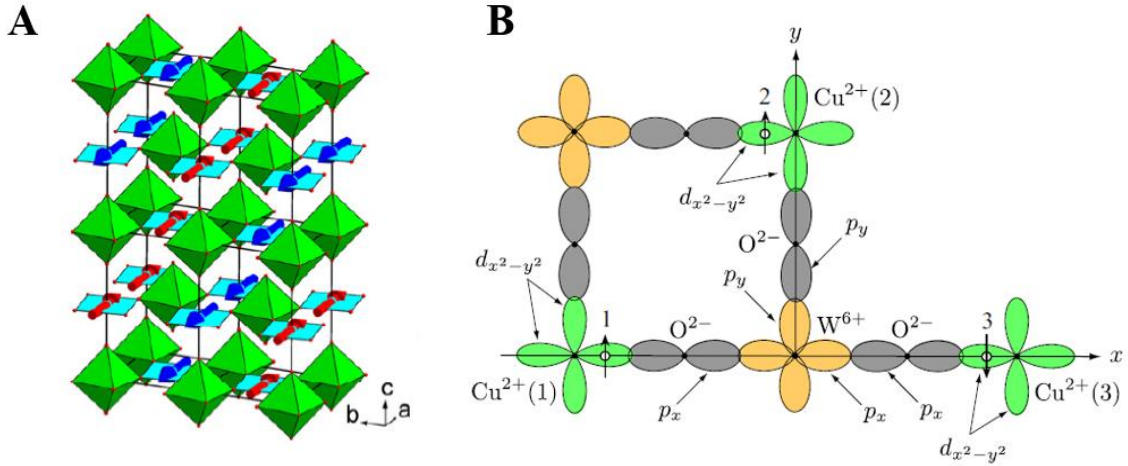


Fig. 5 Magnetic structure and orbital configurations of Sr_2CuWO_6 .

(A) The columnar order magnetic structure with a wave vector $\mathbf{q}_m = (0, 1/2, 1/2)$. (B) The electron orbital configurations related to $\text{Cu}^{2+} - \text{O}^{2-} - \text{W}^{6+} - \text{O}^{2-} - \text{Cu}^{2+}$. The figures (A)(B) are extracted from Ref. [45] and Ref. [43], respectively.

aligned antiparallely which indicates an antiferromagnetic interaction between them. The remaining weak antiferromagnetic interaction between $\text{Cu}^{2+}(1)$ and Cu^{2+} comes from the path $\text{Cu}^{2+}(1) - \text{O}^{2-} - \text{O}^{2-} - \text{Cu}^{2+}(2)$ which skips the intermediate W ion.

To determine the interaction strengths in these two compounds, time-of-flight neutron scattering measurements have been carried out [46, 47]. As shown in Fig. 6, both

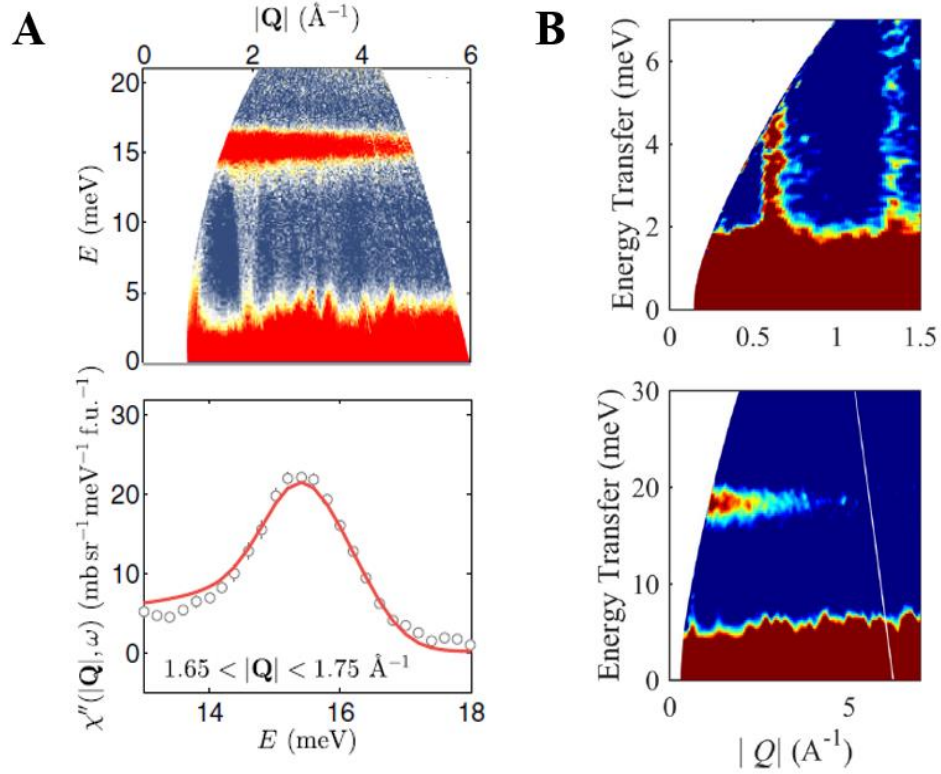


Fig. 6 Magnetic excitations of $\text{Sr}_2\text{CuTeO}_6$ and Sr_2CuWO_6 .

(A) Measured magnetic excitations of $\text{Sr}_2\text{CuTeO}_6$ obtained by subtraction of 120 K from 2 K data using time-of-flight neutron scattering technique (top); a constant- Q cut ($\sim 1.7 \text{ \AA}^{-1}$) of the dynamic susceptibility with the solid red line showing the calculated intensity from spin-wave theory (bottom). (B) Measured magnetic intensity of Sr_2CuWO_6 at 6 K after phonon scattering subtraction with incident neutron energy $E_i = 10 \text{ meV}$ (top) and 45 meV (bottom). The figures (A)(B) are extracted from Ref. [46] and Ref. [47], respectively.

samples exhibit spin-wave like spectra features. Linear spin-wave theory calculations have been performed to reproduce the measured spectra. In $\text{Sr}_2\text{CuTeO}_6$ [46], the nearest-neighbor interaction (J_1) is determined as $-7.60(3)$ meV and J_2 to be $-0.60(3)$ meV. Whereas in Sr_2CuWO_6 [47], the optimized J_1 is -1.2 meV and J_2 is -9.5 meV. The measured data and reproduced calculations confirmed the different types of major interactions in the two parent compounds.

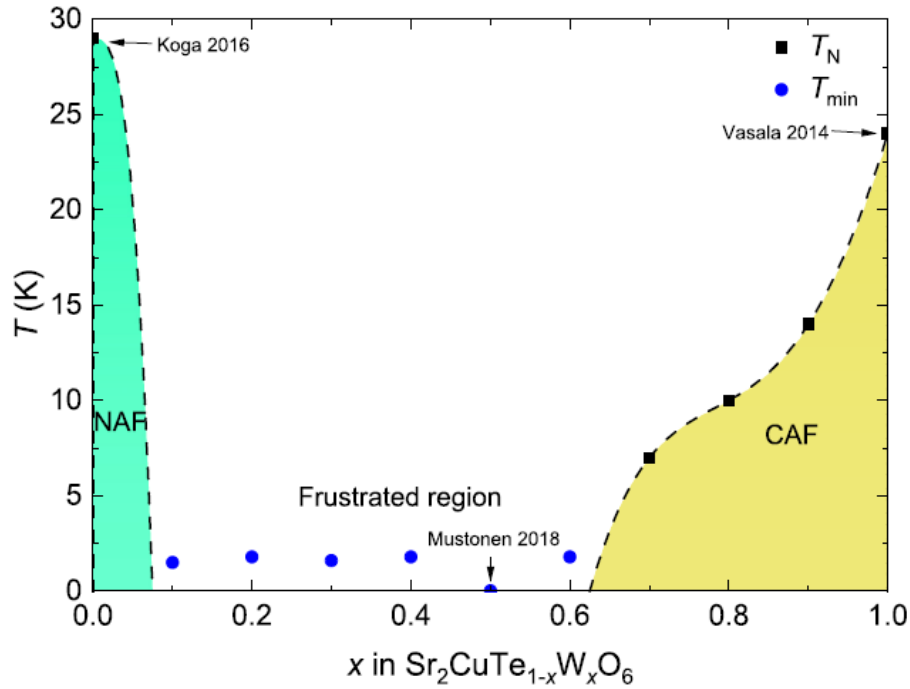


Fig. 7 Schematic phase diagram of $\text{Sr}_2\text{CuTe}_{1-x}\text{W}_x\text{O}_6$.

The black squares represent the measured Neel temperatures and the blue circles represent the lowest temperature measured for samples that remain dynamic. The figure is extracted from Ref. [44].

After the characterization of the two parent compounds, people get more interested in the mixed compounds ($0 < x < 1$). By using muon spin rotation and relaxation method, Mustonen et al. [44, 48] characterized this full isostructural compound series which showed that when $x = 0.1 \sim 0.6$, the system exhibits no long-range magnetic order down to 1.5 K, especially for $x = 0.5$ where spins remain dynamic down to 19 mK (see Fig. 7 the phase diagram). Here, we emphasize that the muon spin rotation and relaxation method is a local probing technique and cannot tell us much about the global space and time correlations. Thus, we do not rely much on these results when we study the concentration-dependent magnetic properties of this compound series. What's more, a specific heat study on $x = 0.5$ compound shows an anomaly in its temperature dependence, i. e. above ~ 1.5 K it is nearly linear in T while below 1.5 K it becomes quadratic to T [49]. This behavior signatures a possible magnetic phase transition into a frozen state below 1.5 K. In order to resolve the puzzling results indicated by the μ SR and specific heat measurements, our group performed temperature-dependent time-of-flight measurements on $x = 0.5$ with three different neutron incident energies, E_i , using two different spectrometers at the Spallation Neutron Source (SNS) located at the Oak Ridge National Laboratory; $E_i = 1.55$ and 3.32 meV were used at the Cold Neutron Chopper Spectrometer (CNCS) [50] to focus on low energy excitations, and $E_i = 45$ meV at the Fine-Resolution Fermi Chopper Spectrometer (SEQUOIA) [51] to probe high energy excitations up to the top of the magnetic energy band. We covered the critical temperature with the temperature range 0.25 K to 12 K with $E_i = 1.55$ meV which offers an excellent energy resolution of $\Delta E_{HWHM} = 0.02$ meV.

2.1 Magnetic excitation spectra

Fig. 8 shows color contour maps of the inelastic neutron scattering cross section, $S(Q, \hbar\omega)$, as a function of momentum transfer, Q , and $\hbar\omega$, acquired at 0.25 K with $E_i = 1.55$ and 3.32 meV, and at 5 K with $E_i = 45$ meV. The $E_i = 45$ meV data are shown only down to ~ 3 meV which corresponds to ~ 35 K and the magnetic excitations above 3 meV are expected to be similar at 5 K and 0.25 K. The figure shows that the magnetic excitations extend from at least 0.05 meV up to 20 meV. The intensity was normalized to obtain $S(Q, \hbar\omega)$ in an absolute unit of $1/\text{meV}/\text{Cu}^{2+}$ by comparing the nuclear Bragg reflections to the calculated nuclear structure factors [41] (see details in Appendix. 1). The total signal from 0.05 to 20 meV, $\frac{\int_{\text{BZ}} \int_{0.05 \text{ meV}}^{20 \text{ meV}} S(Q, \hbar\omega) / [f(Q)]^2 d(\hbar\omega) dQ}{\int_{\text{BZ}} dQ}$, where $f(Q)$ is the Cu^{2+} magnetic form factor, was estimated to be 0.5(1) which is consistent with the sum rule for the isotropic spin of $\frac{2}{3}S(S + 1) = 0.5$.

As shown in the Fig. 8 (A), for $\hbar\omega \lesssim 7$ meV the magnetic excitations exhibit a prominent peak at $Q \sim 0.6 \text{ \AA}^{-1}$. On the other hand, for $\hbar\omega \gtrsim 7$ meV the magnetic excitations are almost featureless in Q , which is due to the Van Hove singularity of the top of the magnetic energy band from a powder sample. These overall features of $S(Q, \hbar\omega)$ can be understood as being due to a powder-averaged spin wave spectrum in a long range ordered magnetic state, similarly to the $S(Q, \hbar\omega)$ reported for the two mother compounds $\text{Sr}_2\text{CuTeO}_6$ [46] and Sr_2CuWO_6 [47], both of which exhibit long range order long range at low temperatures even though their ordered magnetic structures are different.

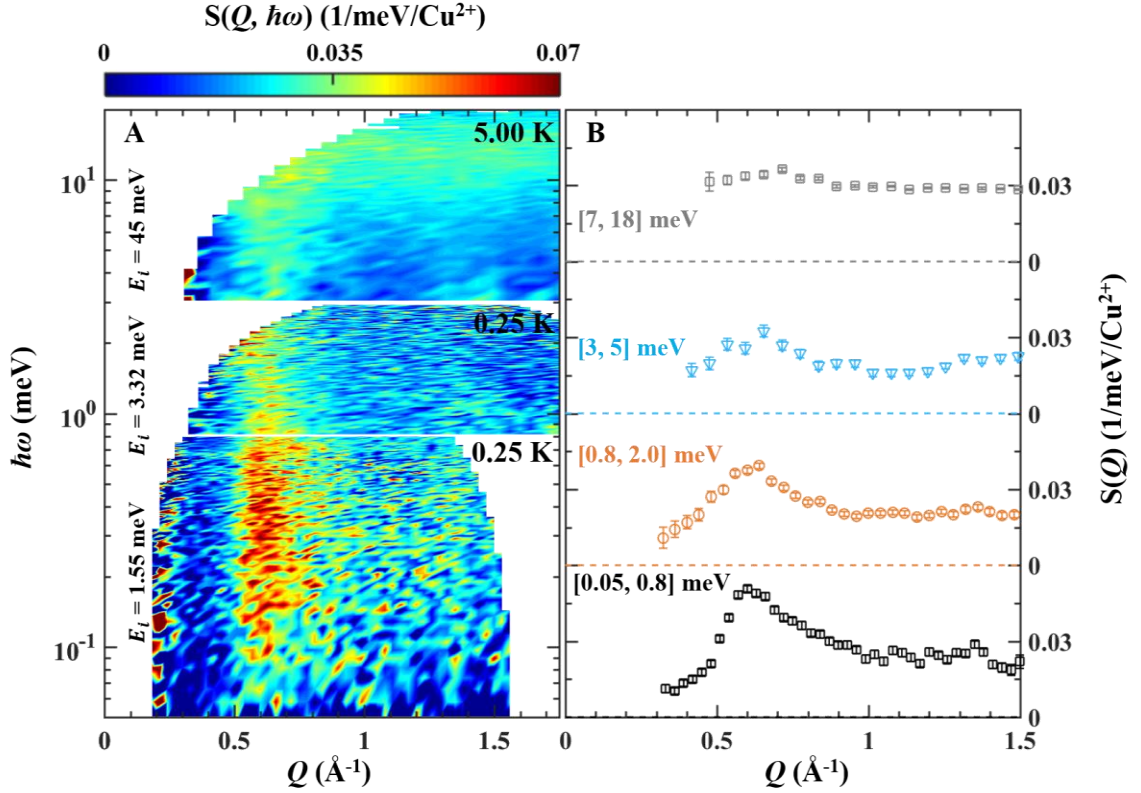


Fig. 8 Inelastic neutron scattering data of $\text{Sr}_2\text{CuTe}_{0.5}\text{W}_{0.5}\text{O}_6$ [52].

(A) Color contour maps of the neutron scattering intensity as a function of momentum transfer, Q , and energy transfer, $\hbar\omega$, measured with three different energies of incident neutrons, $E_i = 1.55$ meV (bottom), 3.32 meV (middle) and 45 meV (top). The $E_i = 1.55$ and 3.32 meV were collected at the Cold Neutron Chopper Spectrometer (CNCS) and the $E_i = 45$ meV data were collected at the Fine-Resolution Fermi Chopper Spectrometer (SEQUOIA) at SNS. (B) Q -dependence of the inelastic neutron scattering intensity, $S(Q) = \frac{\int S(Q, \hbar\omega) d(\hbar\omega)}{\int d(\hbar\omega)}$, for four different $\hbar\omega$ integration ranges. The dashed lines represent the zero values of the corresponding constant- $\hbar\omega$ cuts.

If we closely examine the data of $\text{Sr}_2\text{CuTe}_{0.5}\text{W}_{0.5}\text{O}_6$, however, we notice a peculiar feature. Fig. 8 (B) shows the constant $\hbar\omega$ cuts of $S(Q, \hbar\omega)$, $S(Q)$, for four different energy ranges. For $\hbar\omega \gtrsim 0.8$ meV, $S(Q)$ shows long ranged spin-wave-like features as discussed

above, exhibiting a prominent peak at $Q \sim 0.6 \text{ \AA}^{-1}$ for $\hbar\omega \lesssim 7 \text{ meV}$ and being almost featureless for $\hbar\omega \gtrsim 7 \text{ meV}$. Note that $S(Q)$ for both $3 \leq \hbar\omega \leq 5 \text{ meV}$ (blue triangles) and $0.8 \leq \hbar\omega \leq 2 \text{ meV}$ (orange circles) are more or less symmetric about $Q \sim 0.62 \text{ \AA}^{-1}$. On the other hand, the $S(Q)$ for $0.05 \leq \hbar\omega \leq 0.8 \text{ meV}$ (black squares) is strikingly asymmetric in Q . This indicates that the very low energy spin fluctuations of $\text{Sr}_2\text{CuTe}_{0.5}\text{W}_{0.5}\text{O}_6$ are due to low-dimensional dynamic spin fluctuations. The dimensional crossover of the spin fluctuations from being three-dimensional to lower-dimensional and the low-dimensional low-energy spin fluctuations may hold a key in understanding the anomalous low temperature magnetic properties that previous studies reported for this system [44, 48, 49]. The focus of this work is to examine how the low energy excitations below $\hbar\omega \sim 0.8 \text{ meV}$ evolve as a function of temperature down to sub-K.

The TOF measurements with $E_i = 1.55 \text{ meV}$ were performed at nine different temperatures from 0.25 K to 12 K. Among them, Fig. 9 shows the $S(Q, \hbar\omega)$ for four temperatures, 7, 4, 1.7, and 0.25 K. At all temperatures, the low energy excitations are dominated by the gapless streak that is centered at $Q \sim 0.62 \text{ \AA}^{-1}$. The measured scattering intensity indicates that the system is gapless down to the lowest energy $\hbar\omega \sim 0.05 \text{ meV}$ that can be accessed by the instrument energy resolution. Upon cooling from 7 K to 1.7 K, $S(Q, \hbar\omega)$ increases in strength for low energies of $\hbar\omega < 0.3 \text{ meV}$, and the spectral weight of $S(Q, \hbar\omega)$ gradually shifts to lower energies. Surprisingly, however, upon further cooling from 1.7 K to 0.25 K, the strong low energy spin fluctuations below 0.2 meV become weak as shown as the red square symbols in Fig. 10 (A). The depletion of $S(Q, \hbar\omega)$ at low energies upon cooling is typically a signature of spin freezing or development of static order of spins.

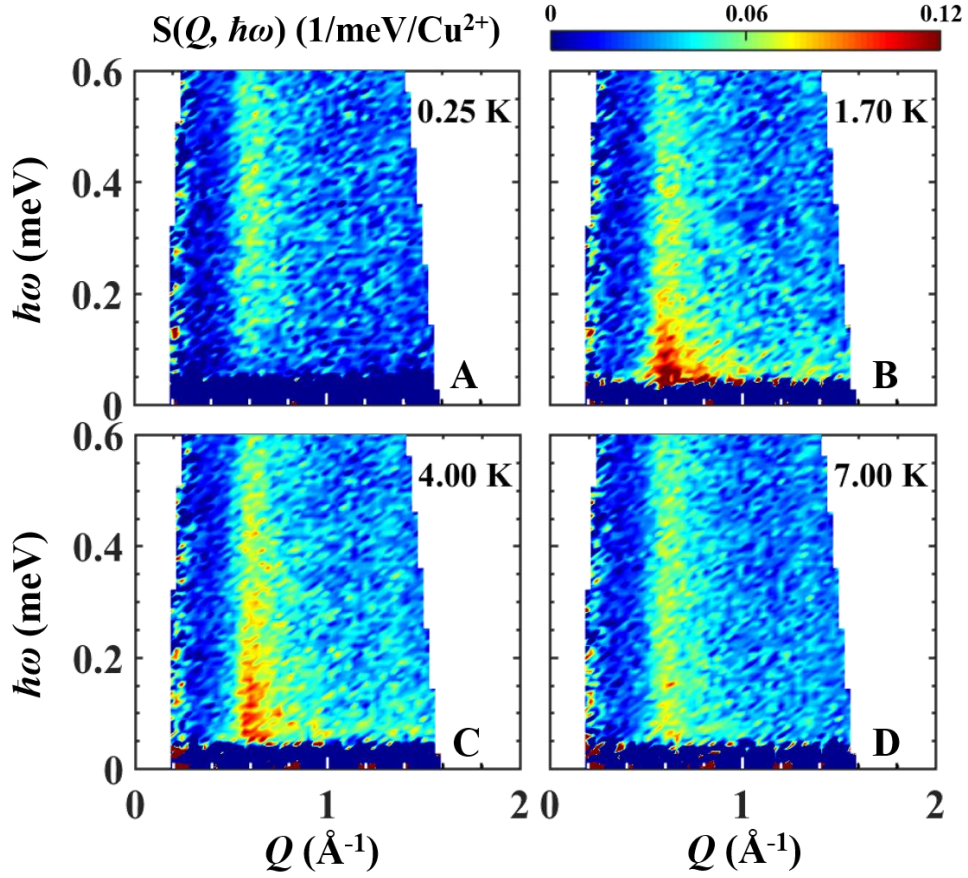


Fig. 9 Low energy spin fluctuations of $\text{Sr}_2\text{CuTe}_{0.5}\text{W}_{0.5}\text{O}_6$. [52]

Color contour maps of the low energy magnetic neutron scattering cross section, $S(Q, \hbar\omega)$, measured with $E_i = 1.55$ meV, measured at (A) 0.25 K, (B) 1.70 K, (C) 4.00 K, and (D) 7.00 K. The temperature independent background was determined by an algorithm (Appendix. 1) using the detailed balance condition, $S(Q, -\hbar\omega) = e^{-\frac{\hbar\omega}{k_B T}} S(Q, \hbar\omega)$, and subtracted from the raw data to get $S(Q, \hbar\omega)$.

In order to investigate how the spectral weight of the low energy spin fluctuations evolve upon cooling, we integrated the scattering cross-section $\tilde{S} \equiv \int_{0.4 \text{ \AA}^{-1}}^{1.0 \text{ \AA}^{-1}} \int_{0.05 \text{ meV}}^{0.2 \text{ meV}} S(Q, \hbar\omega) / [f(Q)]^2 d(\hbar\omega) dQ$ over a range of Q and $\hbar\omega$ covering the prominent low energy peak centered at 0.6 \AA^{-1} and plotted it as a function of T . As shown

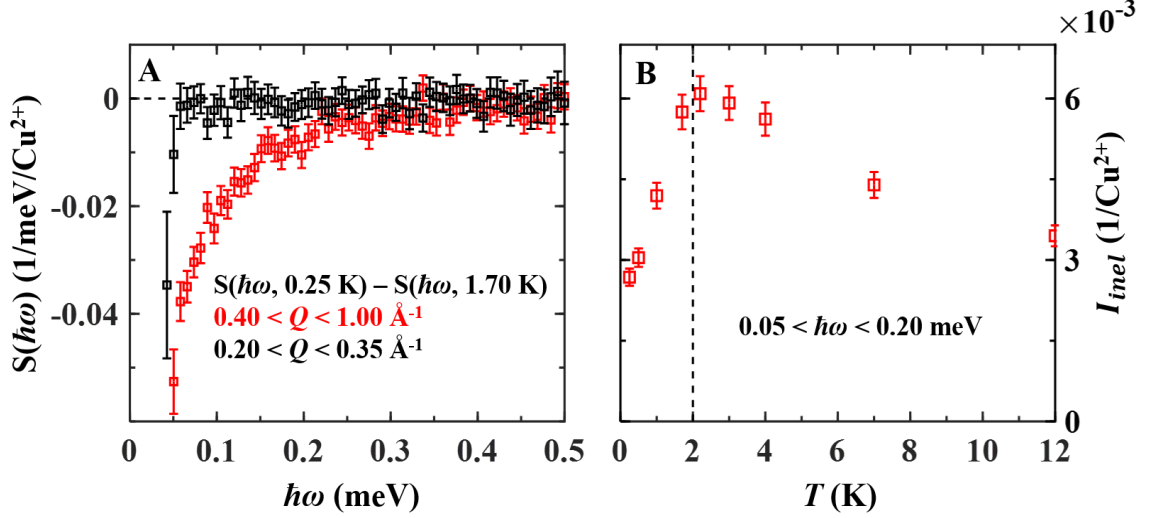


Fig. 10 Low energy spin fluctuations and spectral weights of $\text{Sr}_2\text{CuTe}_{0.5}\text{W}_{0.5}\text{O}_6$. [52]

(A) The Q -averaged neutron scattering intensity, $S(\hbar\omega) = \frac{\int S(Q, \hbar\omega) dQ}{\int dQ}$, obtained with $E_i = 1.55$ meV at 0.25 K is shown after $S(\hbar\omega)$ at 1.7 K was subtracted. The Q -integration range for the red squares was $0.4 \text{ \AA}^{-1} < Q < 1.0 \text{ \AA}^{-1}$ including $q_m = (\frac{1}{2}, 0, 0)$, while that for the black squares was $0.2 \text{ \AA}^{-1} < Q < 0.35 \text{ \AA}^{-1}$ below q_m . (B) the red squares represent the integrated spectral weights over an energy range of $0.05 < \hbar\omega < 0.20$ meV and a Q range of $0.4 \text{ \AA}^{-1} < Q < 1.0 \text{ \AA}^{-1}$ as a function of temperature, $I_{inel} = \tilde{S} \equiv \int_{0.4 \text{ \AA}^{-1}}^{1.0 \text{ \AA}^{-1}} \int_{0.05 \text{ meV}}^{0.20 \text{ meV}} S(Q, \hbar\omega) / [f(Q)]^2 d(\hbar\omega) dQ$.

as the red square symbols in Fig. 10 (B), as T decreases from 12 K to 2 K, the low energy spin fluctuations \tilde{S} get gradually stronger. When T decreases further from 2 K, however, the low energy spin fluctuations gradually weaken, transferring to the elastic channel (see Fig. 11). This strongly indicates that the spins indeed freeze below $T_f \sim 1.7(1)$ K. These findings starkly contradict the previous muon spin relaxation (μSR) study that reported a spin liquid state down to 19 mK [48]. How could the μSR measurements not be able to detect the spin freezing? The clue comes from the fact that the spin freezing is very weak: as shown in Fig. 10 (B), the frozen spectral weight is $\Delta\tilde{S} = \tilde{S}(2 \text{ K}) - \tilde{S}(0.25 \text{ K}) \cong 0.003$

in the unit of $1/\text{Cu}^{2+}$. Thus, below T_f only 0.6 % out of the total spectral weight of the isotropic spin that is $\frac{2}{3}S(S + 1) = 0.5$ is frozen and the rest is fluctuating.

In order to study the nature of the weak spin freezing, we plotted the elastic magnetic scattering cross-section, $S_{elas}^{mag}(Q, 0.25 \text{ K}) = \int_{-0.02 \text{ meV}}^{0.02 \text{ meV}} S(Q, \hbar\omega) d(\hbar\omega)$ measured at 0.25 K, after background subtraction. Here, background was determined by averaging similar elastic $S_{elas}(Q)$ measured at three different temperatures 4 K, 7 K, and

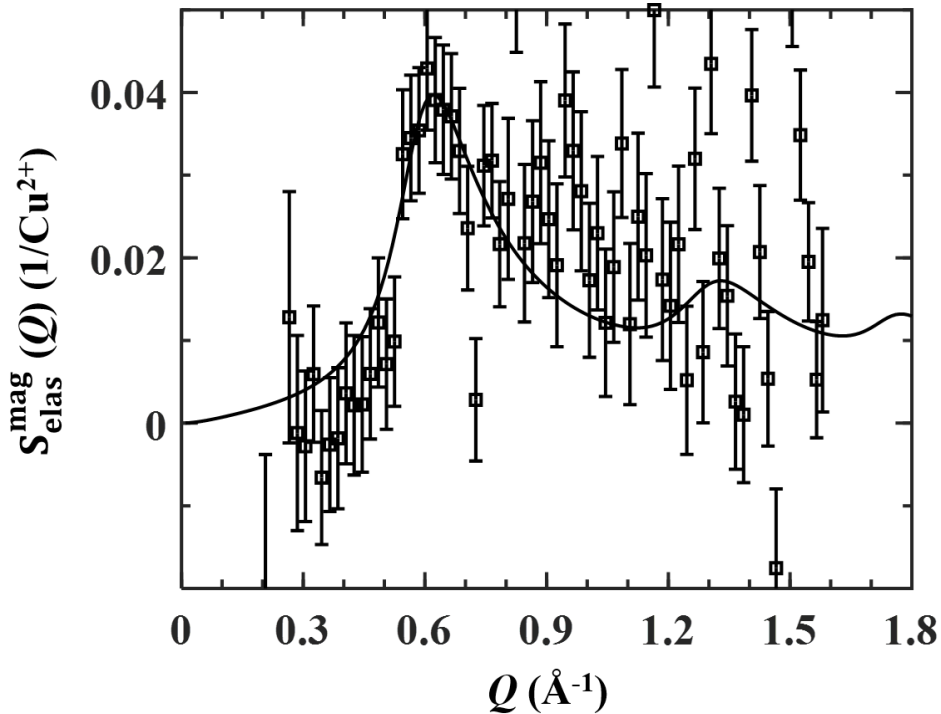


Fig. 11 The elastic magnetic scattering cross section of $\text{Sr}_2\text{CuTe}_{0.5}\text{W}_{0.5}\text{O}_6$. [52]

The elastic magnetic scattering signal $S_{elas}^{mag}(Q, 0.25 \text{ K}) = \int_{-0.02 \text{ meV}}^{0.02 \text{ meV}} S(Q, \hbar\omega) d(\hbar\omega)$ was measured at 0.25 K after background subtraction. Here background was determined by averaging similar elastic $S_{elas}(Q)$ measured at three different temperatures 4 K, 7 K, and 12 K above T_f , to increase the statistics. The black solid line is the fit to the phenomenological model discussed later in the text.

12 K above T_f , to increase the statistics. As shown in Fig. 11, $S_{elas}^{mag}(Q, 0.25 \text{ K})$ exhibits an asymmetric broad peak at $Q \sim 0.62 \text{ \AA}^{-1}$ similar to the low energy gapless excitations shown in Fig. 12. This implies that the static correlations of the frozen spins are basically the same as the dynamic correlations of the fluctuating moments. The black line is the fit to a phenomenological Lorentzian function with a two-dimensional correlation length of $\xi = 12(6) \text{ \AA}$ that will be explained in detail later. The large error of ξ is due to the weak signal and poor statistics.

2.2 Spatial correlations

To investigate the nature of the critical spin fluctuations at low energies, we have generated constant- Q and constant- $\hbar\omega$ cuts from $S(Q, \hbar\omega)$ taken at nine different temperatures spanning the spin freezing transition. $S(\hbar\omega)$ was then converted to the imaginary part of the dynamic susceptibility $\chi''(\hbar\omega)$ using the fluctuation-dissipation theorem.

First, shown in Fig. 12, note that $S(Q)$ exhibits a prominent asymmetric peak with a maximum at $Q \approx 0.62 \text{ \AA}^{-1}$ that corresponds to $\mathbf{q}_m = (\frac{1}{2}, 0, 0)$, a sharp edge at lower Q s, and a long tail at higher Q s. There is another peak at $Q \approx 1.3 \text{ \AA}^{-1}$ that corresponds to $\mathbf{q}_m = (\frac{1}{2}, 1, 0)$. Thus, the low energy spin fluctuations have a characteristic antiferromagnetic wavevector of $\mathbf{q}_m = (\frac{1}{2}, 0, 0)$. For a quantitative analysis of the spin dynamical correlation, we fit $S(Q)$ to the product of the independent lattice-Lorentzian functions [53, 54],

$$\frac{d\sigma(\mathbf{Q})}{d\Omega} \propto |F_m^\perp(\mathbf{Q})|^2 \prod_{\alpha} \frac{\sinh(\xi_{\alpha}^{-1})}{\cosh(\xi_{\alpha}^{-1}) - \cos[(\mathbf{q}_m - \mathbf{Q}) \cdot \hat{\mathbf{r}}_{\alpha}]}.$$

(Eq. 12)

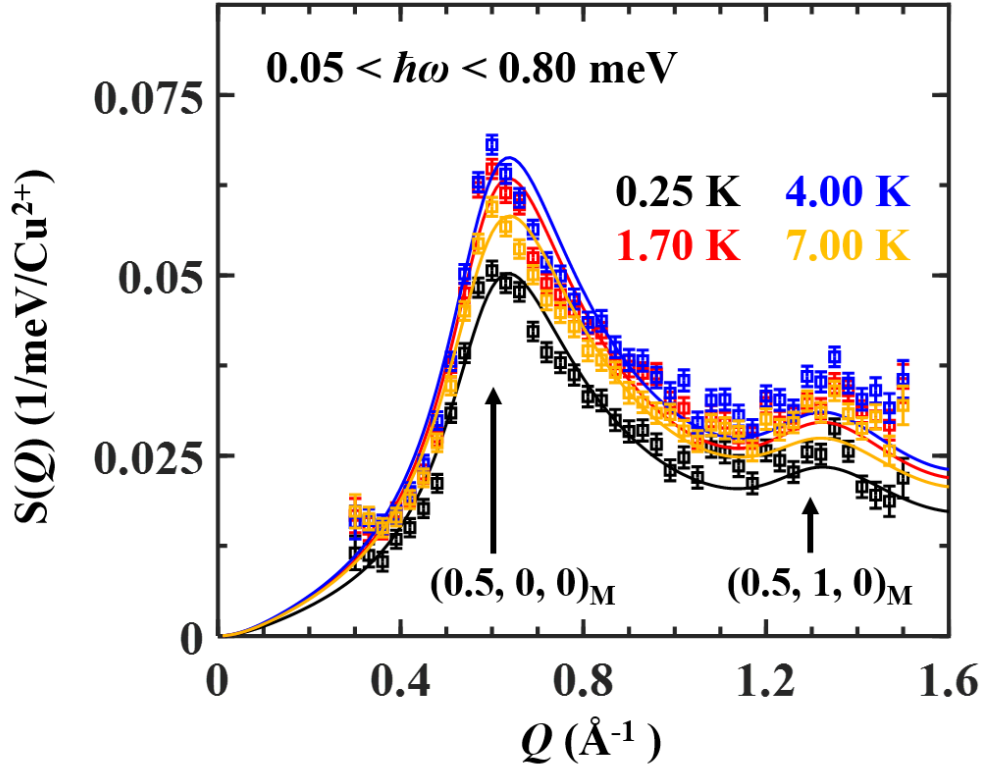


Fig. 12 Q -dependence of low energy spin fluctuations in $\text{Sr}_2\text{CuTe}_{0.5}\text{W}_{0.5}\text{O}_6$. [52]

The Q -dependence of the low energy neutron scattering intensity was obtained by

$$\text{averaging } S(Q, \hbar\omega) \text{ over } 0.05 < \hbar\omega < 0.80 \text{ meV, } S(Q, \hbar\omega) = \frac{\int_{0.05 \text{ meV}}^{0.80 \text{ meV}} S(Q, \hbar\omega) d(\hbar\omega)}{\int_{0.05 \text{ meV}}^{0.80 \text{ meV}} d(\hbar\omega)},$$

at four different temperatures, 0.25 K (black squares), 1.70 K (red), 4.00 K (blue), and

7.00 K (orange). The color-coded solid lines are the $S(Q)$ fitting results to the

Lorentzian function Eq. 12. Two characteristic wave vectors, $\mathbf{q}_m = \left(\frac{1}{2}, 0, 0\right)$ and

$\left(\frac{1}{2}, 1, 0\right)$, are indexed with black arrows.

Here $F_m^\perp(\mathbf{Q}) = f(Q)\sum_\nu \mathbf{M}_\nu^\perp e^{-i\mathbf{Q}\cdot\mathbf{r}_\nu}$, where \mathbf{M}_ν and \mathbf{r}_ν are the staggered magnetic moment and the position of a Cu^{2+} ion at the site ν , respectively, and $f(Q)$ is the Cu^{2+} magnetic form factor. ξ_α and \hat{r}_α are the spin-correlation length and the unit cell lattice vector along the crystallographic axis ($\alpha = a, b, c$), respectively. The detailed parameter settings can be found in Appendix. 1. The scattering cross-section was convoluted with the instrumental resolution to fit the data. In the fitting, we used two different correlation lengths, an isotropic in-plane correlation length, $\xi = \xi_a = \xi_b$, and an out-of-plane correlation length, ξ_c . The fitting results are shown as the color-coded solid lines in Fig. 12. For all the low temperatures considered, the out-of-plane ξ_c was negligible, confirming the two-dimensionality of the critical spin fluctuations. Furthermore, as shown as black triangles in Fig. 14, the in-plane correlation length, ξ , is very short, $\xi = 8.4(9) \text{ \AA} \sim \sqrt{2} d_{NN}$ at 0.25 K, in which d_{NN} is the distance between the nearest neighboring Cu^{2+} ions. And ξ gets slightly shorter above T_f : $\xi = 7.1(8) \text{ \AA}$ at 12 K. Thus, the critical spin fluctuations at low temperatures have very short two-dimensional correlations that fall off quickly when the distance between the spins goes beyond the distance between the second nearest neighbors.

2.3 Dynamic susceptibility

Fig. 13 shows $\chi''(\hbar\omega)$. At 7 K which is far below the Curie-Weiss temperature of $\text{Sr}_2\text{CuTe}_{0.5}\text{W}_{0.5}\text{O}_6$, $|\Theta_{CW}| = 71 \text{ K}$ [48] and well above T_f , the system is in a spin liquid state. In this state, as shown as the orange squares, $\chi''(\hbar\omega)$, obtained by the fluctuation-

dissipation theorem $\chi''(\hbar\omega) = \frac{1}{\pi} \left(1 - e^{-\frac{\hbar\omega}{k_B T}}\right) S(\hbar\omega)$, gradually increases with increasing $\hbar\omega$. Upon cooling down to $1.7 \text{ K} \approx T_f$, $\chi''(\hbar\omega)$ softens, i.e., the spectral weight gradually

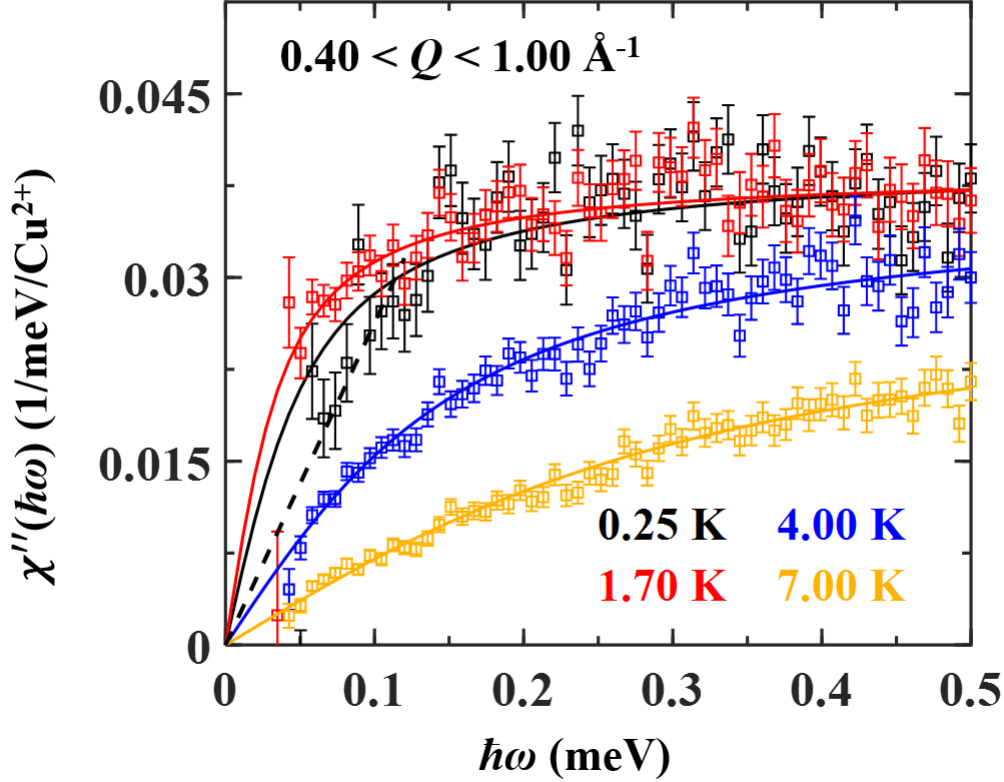


Fig. 13 $\hbar\omega$ -dependence of low energy spin fluctuations in $\text{Sr}_2\text{CuTe}_{0.5}\text{W}_{0.5}\text{O}_6$. [52]

The color squares are the energy dependence of the imaginary part of the dynamic susceptibility, $\chi''(\hbar\omega) = \left(1 - e^{-\frac{\hbar\omega}{k_B T}}\right) S(\hbar\omega)$, obtained by averaging and converting the inelastic neutron scattering intensity $S(Q, \hbar\omega)$ over $0.40 < Q < 1.00 \text{ \AA}^{-1}$, i.e.

$$S(\hbar\omega) = \frac{\int_{0.40 \text{ \AA}^{-1}}^{1.00 \text{ \AA}^{-1}} S(Q, \hbar\omega) dQ}{\int_{0.40 \text{ \AA}^{-1}}^{1.00 \text{ \AA}^{-1}} dQ}, \text{ at } 0.25 \text{ K (black), } 1.70 \text{ K (red), } 4.00 \text{ K (blue), and } 7.00 \text{ K}$$

(orange). The color solid lines represent fits by the spectral weight function of an arctangent type, $y = y_0 \tan^{-1}(\hbar\omega/\Gamma_{\min})$, which gives the lower bound (Γ_{\min}) of the spin relaxation rates. The black dashed line represents the linear $\hbar\omega$ dependence of low energy fluctuations up to $\sim 0.15 \text{ meV}$.

shifts to lower energies. This low energy behavior is expected for a spin liquid since the energy scale of the low energy spin fluctuations in a spin liquid is temperature, $k_B T$, where $k_B \approx 0.086$ meV/K is the Boltzmann constant. For a quantitative analysis of the low energy fluctuations, we compare $\chi''(\hbar\omega)$ to a phenomenological function, $\chi''(\hbar\omega) \propto \tan^{-1}\left(\frac{\hbar\omega}{\Gamma_{min}}\right)$, that assumes a broad distribution of spin relaxation rates with the lower limit

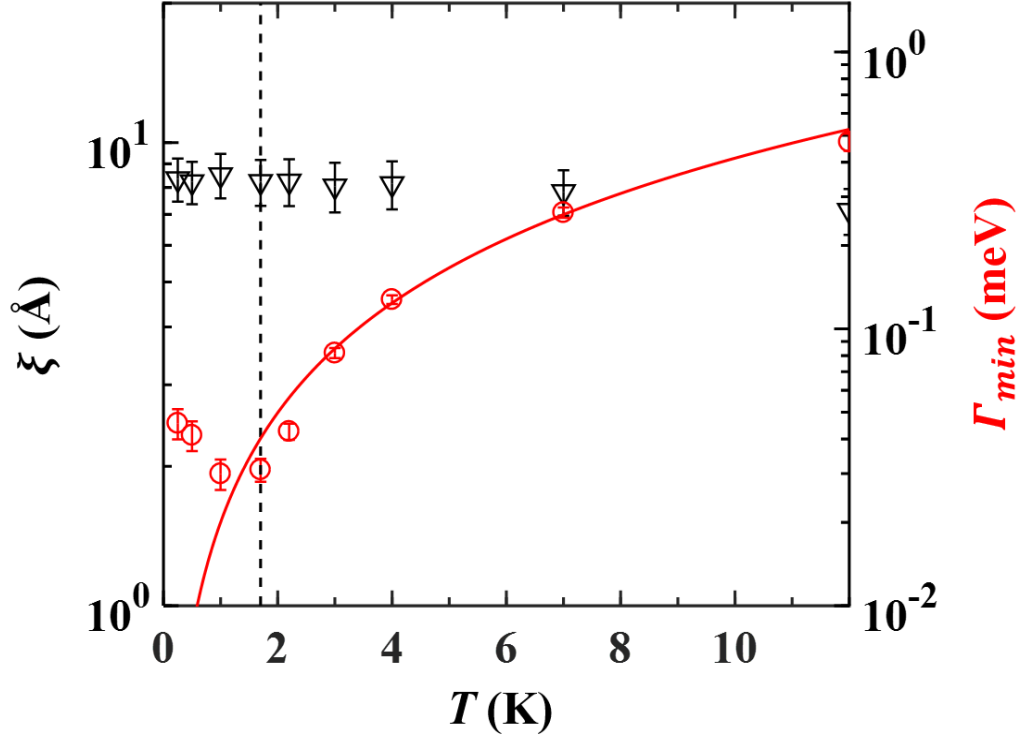


Fig. 14 Spin correlation length and relaxation rate of the low energy spin fluctuations in $\text{Sr}_2\text{CuTe}_{0.5}\text{W}_{0.5}\text{O}_6$. [52]

The black triangles are the correlation length, ξ , extracted from the $S(Q)$ fitting in Fig. 12. The red circles are the lower limit of the spin relaxation rates, Γ_{min} , extracted from the $y = y_0 \tan^{-1}(\hbar\omega/\Gamma_{min})$ fitting of the imaginary part of the dynamic susceptibility, $\chi''(\hbar\omega)$, as a function of temperature. The red solid line represents the fitting results $\frac{\Gamma_{min}}{|J|} = \left(\frac{k_B T}{|J|}\right)^\alpha$ as discussed in the text.

of Γ_{min} [55]. Fig. 14 shows the resulting Γ_{min} in a log scale as a function of T (see red circles). The red line is a fit to a function, $\frac{\Gamma_{min}}{|J|} = \left(\frac{k_B T}{|J|}\right)^\alpha$, with an energy scale of the magnetic interactions, $|J| = 9(2)$ meV, and a power, $\alpha = 1.3(1)$. The value of $|J|$ is close to the previously-reported value of the dominant magnetic interaction in this system [56], $J_2 \sim -9$ meV. However, upon further cooling below T_f , low-energy spin degrees of freedom get depleted in the frozen state (Fig. 10 (B)) where $\chi''(\hbar\omega) \propto \hbar\omega$ up to $k_B T_f \approx 0.15$ meV, as shown as the black squares and black dashed line in Fig. 13. The linear behavior of $\chi''(\hbar\omega) \propto \hbar\omega$ for $\hbar\omega < k_B T_f$ is consistent with the quadratic behavior of specific heat [49], $C(T) \propto T^2$ for $k_B T < k_B T_f$.

2.4 Spin jam state

In a previous experimental study, the state above T_f was regarded as a valence-bond glass (VBG) [49, 57, 58]. The magnetic excitations, however, do not exhibit any singlet-to-triplet-excitations characteristic of valence bonds (see Fig. 8 and Refs. [14-16, 18]). Rather, the magnetic excitations at high energies resemble spin-wave excitations of the ordered state of Sr_2CuWO_6 , even though the excitations are smeared in energy [47, 56]. Thus, we believe it is more appropriate to call the state of $\text{Sr}_2\text{CuTe}_{0.5}\text{W}_{0.5}\text{O}_6$ above T_f a disorder-induced glassy SL rather than VBG. Below T_f , $\chi''(\hbar\omega) \propto \hbar\omega$ and $C_v(T) \propto T^2$. Such behavior is consistent with linearly dispersing modes with density of state $\rho(\omega) \propto \omega^{D-1}$ where D is the magnetic dimensionality. In systems with rotationally invariant interactions, such modes appear as Goldstone modes that are a consequence of a

spontaneous symmetry breaking into a long range ordered state. However, such linearly dispersing modes can appear even in symmetry broken states without long range order, and such modes in Heisenberg spin glasses are called Halperin-Saslow (HS) modes [59, 60]. These suggest that the frozen state is a quantum analog of a spin jam state, a glassy state typical for non-dilute frustrated magnets [61]. The spin jam is a distinct state from an ordinary spin glass of diluted magnets. The low energy spin dynamics of a spin jam is governed by the HS modes while those of a spin glass is by localized two-level energy states [59-61], leading to different memory effects [62]. The main assumptions in the Halperin-Saslow theory are the presence of some freezing as well as nonvanishing spin stiffness [59]. While the Halperin-Saslow scenario is an appealing direction to explain the experimental observations, it is unknown how effective such a mechanism can be in our system where the frozen moment is very small, $\langle S \rangle / S \sim 0.1$. This presents a theoretical challenge to fully understand the mechanism of the freezing of the disorder-induced SL and the possible extension of HS theory into this new highly fluctuating quantum regime.

Chapter 3

(BA)₂PbI₄ & (PEA)₂PbI₄: Structural Dynamics and Optoelectronic Properties

3.1 Experimental techniques

3.1.1 sample preparation

For this work, powder samples of (BA)₂PbI₄ and (PEA)₂PbI₄ were used.

(BA)₂PbI₄. The synthesis of the (BA)₂PbI₄ powder sample was adopted from the method reported by Stoumpos *et al.* [63]. PbI₂ was dissolved in a mixture of HI and H₃PO₂ under heating. An equal molar of BAI was then added to the solution. After dissolution, the heating and stirring were discontinued and the solution was left to cool to room temperature, when (BA)₂PbI₄ crystalized into orange plates. The crystals were collected by suction filtration and washed three times with ethyl ether before vacuum-dried overnight.

(PEA)₂PbI₄. For the preparation of the (PEA)₂PbI₄ powder samples, stoichiometric amounts of phenylethylamine iodide (Greatcell Solar) and lead iodide (99.9985%, Alfa Aesar) were dissolved in γ -Butyrolactone ($\geq 99\%$, Sigma Aldrich) and stirred overnight. This solution was then added dropwise into toluene (anhydrous, 99.8%, Sigma Aldrich) which acts as an antisolvent. This mixture was then sonicated to further crash out the perovskite powder. After centrifuging at 3000 rpm for 5 minutes, the supernatant was poured out. New toluene was added. This centrifuge and wash procedure

were repeated several times. Finally, the resulting powder was dried in vacuum overnight.

All the samples were synthesized in the Choi Laboratory for Optoelectronic Nanomaterials of the Department of Chemical Engineering, University of Virginia.

3.1.2 Neutron scattering measurements

Inelastic neutron scattering. Vibrational dynamics of $(\text{BA})_2\text{PbI}_4$ and $(\text{PEA})_2\text{PbI}_4$ was studied by time-of-flight inelastic neutron scattering (INS) measurements up to 600 meV using 4D-Space Access Neutron Spectrometer (4SEASONS) [64] at J-PARC. To cover the wide range of phonon spectra, six different incident energies (E_i) were used (10, 30, 62, 115, 250, 712 meV). The data were collected during heating from 8 K to 300 K.

Quasi-elastic neutron scattering. The rotational dynamics of both samples was studied by performing quasi-elastic neutron scattering on the powder samples using the cold-neutron disk-chopper spectrometer (AMATERAS) [65] at Japan Proton Accelerator Research Complex (J-PARC). The incident neutron energy E_i was set to be 3.3 meV which can provide an energy resolution of ~ 0.04 meV. The powder samples were loaded into an annular aluminum can which was mounted in a top loading closed cycle refrigerator (TL-CCR). The measurements were performed from 10 K to 300 K.

3.2 Theoretical data analysis and calculations

3.2.1 Density Functional Theory Calculations

Structure relaxation. First-principles density functional theory (DFT) calculations were performed to understand the microscopic nature of the vibrational modes and the experimental INS spectra of $(\text{BA})_2\text{PbI}_4$ and $(\text{PEA})_2\text{PbI}_4$. We used the Vienna ab initio Simulation Package (VASP) with projector augmented wave (PAW) method [66]. The PBE-type (Perdew-Burke-Ernzerhof) generalized gradient approximation is adopted for the exchange-correlation functional [67]. The initial structure of $(\text{BA})_2\text{PbI}_4$ we used in DFT calculations is the orthorhombic ($Pbca$ LT) structure obtained from Rietveld refinement [68]. For $(\text{PEA})_2\text{PbI}_4$, the initial structure (triclinic, $P-1$) we used is obtained from single-crystal X-ray diffraction [69].

Phonon band structure and phonon spectra simulation. The phonon band structures of the two samples were calculated with a $4 \times 4 \times 4$ grid of the phonon momentum space and a $1 \times 1 \times 1$ supercell size due to computing ability limitation. The phonon band structures were calculated along the high-symmetry \mathbf{q} path: $\Gamma(0,0,0) \rightarrow X(1/2, 0,0) \rightarrow S(1/2, 1/2, 0) \rightarrow Y(0, 1/2, 0) \rightarrow \Gamma(0,0,0) \rightarrow Z(0,0, 1/2) \rightarrow U(1/2, 0, 1/2) \rightarrow R(1/2, 1/2, 1/2) \rightarrow T(0, 1/2, 1/2) \rightarrow Z(0,0, 1/2)$ for both samples. Furthermore, the phonon spectra were simulated for both $(\text{BA})_2\text{PbI}_4$ and $(\text{PEA})_2\text{PbI}_4$ using the third-part package, OCLIMAX [70]. Because of the low crystal symmetry (triclinic $P-1$) and large

number of atoms (188 per unit cell) of (PEA)₂PbI₄, imaginary phonon frequencies cannot be removed in DFT calculations, indicating that some intrinsic structure instability exist in this low-symmetry system. The structure instability will not significantly affect the hybrid modes and organic modes which contain less Pb-I lattice vibration than inorganic modes.

Vibrational energy fraction. To understand and characterize the phonon modes, we have calculated the vibrational energy fractions for both samples. Vibrational energy fraction is defined as the energy contribution of each atomic type ($AT = \text{Pb, I, N, C, H}$)

$$F_{AT}(s, \mathbf{q}) = \frac{\sum_{i \in AT} m_i \omega_s(\mathbf{q})^2 |\mathbf{u}_i(s, \mathbf{q})|^2}{\sum_{i \in all} m_i \omega_s(\mathbf{q})^2 |\mathbf{u}_i(s, \mathbf{q})|^2} \quad (\text{Eq. 13})$$

where s and \mathbf{q} represent the phonon mode index and phonon wavevector, respectively. And $\mathbf{u}_i(s, \mathbf{q})$ is the mean square root displacement of the i -th atom due to the activation of phonon mode s . m_i is the mass of the i -th atom, and $\omega_s(\mathbf{q})$ is the eigen frequency of phonon mode s at \mathbf{q} .

3.2.2 Rotational Mode Calculations

The rotation model that accounts for the preferential molecular orientation is called jump model [40, 71]. The rotational dynamics of the organic cation is determined by its own symmetry and the local crystal symmetry. The possible rotational modes are described as the irreducible representations of the direct product $\Gamma = C \otimes M$ where C and M are the point groups of the local crystal symmetry and the molecule symmetry,

respectively. In group theory, the static and dynamic structure factor for rotational motions of molecules in a crystal can be written as [71]

$$S_{cal}(Q, \hbar\omega) = e^{-\langle u^2 \rangle Q^2} \left(\sum_{\gamma} A_{\gamma}(Q) \frac{1}{\pi} \frac{\omega_{\gamma}}{1 + \omega^2 \tau_{\gamma}^2} \right)$$

(Eq. 14)

where the sum over γ runs over all the irreducible representations of the system group Γ , Γ_{γ} ; $e^{-\langle u^2 \rangle Q^2}$ is the Debye Waller factor, $\langle u^2 \rangle$ is the mean squared atomic displacement.

For a polycrystalline sample, $A_{\gamma}(Q)$ is given by [71]

$$A_{\gamma}(Q) = \frac{l_{\gamma}}{g} \sum_{\alpha} \sum_{\beta} \chi_{\gamma}^{\alpha\beta} \sum_{C_{\alpha}} \sum_{M_{\beta}} j_0(Q|R - C_{\alpha}M_{\beta}R|)$$

(Eq. 15)

Here g is the order of group Γ and l_{γ} is the dimensionality of Γ_{γ} . The sums over α and β run over all the classes of C and M , respectively, and the sums over C_{α} and M_{β} run over all the rotations that belong to the crystal class, α , and to the molecule class, β , respectively. The characters of Γ_{γ} , $\chi_{\gamma}^{\alpha\beta}$, are the products of the characters of $C_{\gamma C}$ and $M_{\gamma M}$; $\chi_{\gamma}^{\alpha\beta} = \chi_{\gamma C}^{\alpha} \chi_{\gamma M}^{\beta}$. $j_0(x)$ is the zeroth spherical Bessel function and, $|R - C_{\alpha}M_{\beta}R|$, is the distance between the initial atom position R and final atom position $C_{\alpha}M_{\beta}R$, called the jump distance. The relaxation time for the Γ_{γ} mode, τ_{γ} , is written as [71]

$$\frac{1}{\tau_{\gamma}} = \sum_{\alpha} \frac{n_{\alpha}}{\tau_{\alpha}} \left(1 - \frac{\chi_{\gamma}^{\alpha e}}{\chi_{\gamma}^{Ee}} \right) + \sum_{\beta} \frac{n_{\beta}}{\tau_{\beta}} \left(1 - \frac{\chi_{\gamma}^{E\beta}}{\chi_{\gamma}^{Ee}} \right)$$

(Eq. 16)

where n_α, n_β are the number of symmetry rotations of the classes, α and β , respectively. E and e represent the identity operations of C and M , respectively.

To fit the quasi-elastic neutron scattering spectra, the calculated $S_{cal}(Q, \hbar\omega)$ has to be convoluted with the instrument resolution. The phonon contributions cannot be ignored especially at high T s. Then we have the fitting function as

$$S(Q, \hbar\omega) = A_{rot} \int_{-\infty}^{\infty} S_{cal}(Q, \hbar\omega - \hbar\omega') S_{res}(\hbar\omega') d(\hbar\omega') \\ + A_{vib} Q^2 e^{-(u^2)Q^2}$$

(Eq. 17)

where $S_{res}(\hbar\omega)$ is the instrument resolution function. A_{rot} and A_{vib} are the scaling factors for the rotational contributions and the vibrational contributions.

3.3 Structural Dynamics and Optoelectronic properties

3.3.1 Vibrational Dynamics

The lattice vibrations of these ionic crystals have been reported to play a crucial role in their optoelectronic properties. Previous studies on 3D HOIPs suggest that their exotic optoelectronic properties arise from the extended charge carrier lifetimes, long

carrier diffusion lengths, and carrier protection from defects [72-77]. Relevant microscopic mechanisms include polaron formation (here, polaron is referred as a quasi-particle which is formed by the Coulomb interaction between a free charge carrier and the ionic lattice) [78-85], electron-phonon coupling [37, 86-89], and phonon melting [72, 90, 91]. For example, the electron-phonon coupling, i.e., the interaction between the charge carriers and the lattice vibrations, has been confirmed experimentally to lead to the blue-shift of the electronic band gap in methylammonium lead iodide (MAPbI₃) [92]. Also, the thermally induced changes in the line shape, linewidth, and intensity of the photoluminescence spectrum of various 2D HOIPs were attributed to electron-phonon coupling [37].

The so-called phonon melting describes a phenomenon where the phonon peaks that are well-defined in energy at low temperatures broaden upon heating and finally become a featureless continuum at high temperatures even though the system remains crystalline [91]. It is due to the softness of ionic bonds in the ionic crystals and hence called ‘crystal-liquid duality’. In 3D HOIPs, this lattice ‘softness’, coupled with the highly polar and ionic characters, means an electron or hole can efficiently couple to polar fluctuations and ion displacements, leading to the large polaron formation and the screening of the Coulomb potential. Thus, carrier scattering with charged defects and optical phonons is efficiently screened in the soft ionic perovskite structure [93].

In 2D HOIPs, things could get different due to the fact that majority charge carriers are in the form of excitons with large binding energies, instead of free carriers in 3D HOIPs, due to the strong structure-induced quantum-confinement effects. Thus, investigating the vibrational dynamics in 2D HOIPs is of critical significance to

understanding the possible connections between the lattice vibration and optoelectronic properties of these low-dimensional ionic crystals.

As the starting point of the vibrational dynamics study, the crystal structures of both samples are widely studied via neutron diffraction and single-crystal X-ray diffraction (Fig. 15) [68, 69]. In $(\text{BA})_2\text{PbI}_4$, two structural phases were identified [68]: low-temperature (LT) orthorhombic $Pbca$ phase ($T < 275$ K) and high-temperature (HT) orthorhombic $Pbca$ phase. Besides the different relative magnitude of lattice constants for the two phases, the major difference lies in the orientation of BA^+ molecules, i.e., the tilting angle between the BA^+ chain molecule and the crystallographic c -axis (out-of-

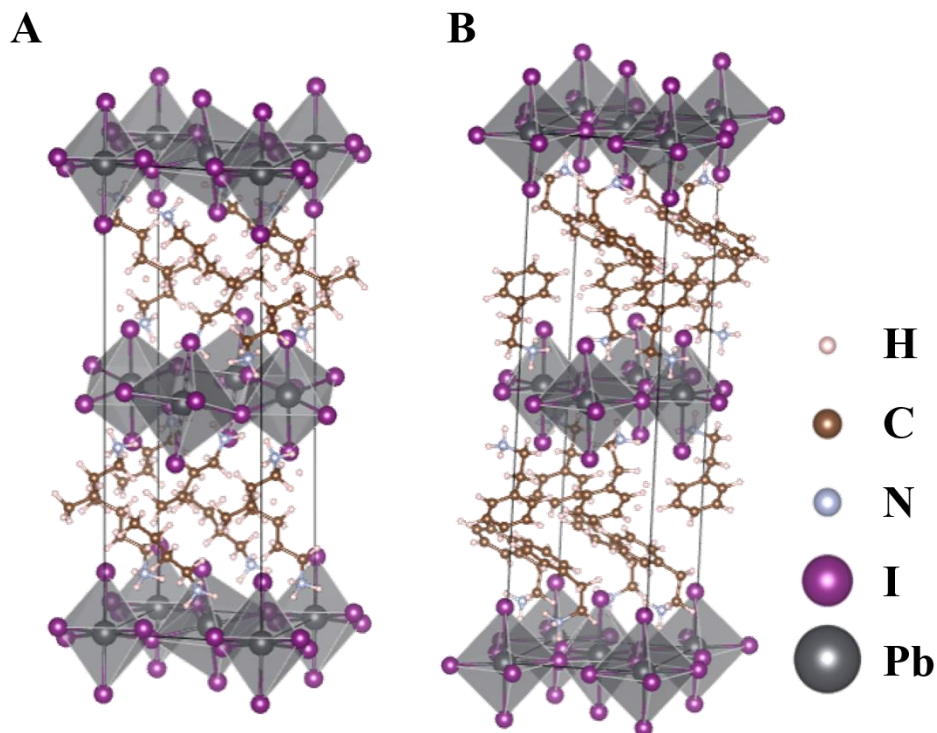


Fig. 15 Schematic of crystal structure of $(\text{BA})_2\text{PbI}_4$ and $(\text{PEA})_2\text{PbI}_4$.

The crystal structure of $(\text{BA})_2\text{PbI}_4$ (A) and $(\text{PEA})_2\text{PbI}_4$ (B). The gray, violet, cyan, brown, and pink spheres represent the Pb, I, N, C, and H atoms, respectively.

perovskite-layer). The tilting angle is $\sim 41^\circ$ in *Pbca* LT phase, while that in *Pbca* HT phase is 28° . The significant difference in the tilting angle will greatly influence the rotational dynamics of molecules in the two phases which will be discussed later. On the other hand, $(\text{PEA})_2\text{PbI}_4$ exhibits a lower crystal symmetry (triclinic *P-1*) with more complicated atomic distributions. Unlike $(\text{BA})_2\text{PbI}_4$ where BA^+ molecules are off-site stacked, PEA^+ molecules are nearly on-site stacked, repulsed by the massive benzene rings. The orientation of PEA^+ molecule also undergoes a rotation between adjacent molecule layers. This peculiar stacking structure is expected to result in dramatically different device performance compared with $(\text{BA})_2\text{PbI}_4$. We will use these crystal structures in our DFT calculations to identify the lattice vibration for both samples.

To investigate the lattice vibrations, we first performed temperature-dependent inelastic neutron scattering (INS) measurements from 8 K up to 300 K at 4SEASON, J-PARC with a series of incident neutron energies ($E_i = 10, 30, 62, 115, 250, 712$ meV) to cover the entire phonon spectra of the two samples. Fig. 16 and Fig. 17 show the vibrational dynamics identification results for $(\text{BA})_2\text{PbI}_4$ and $(\text{PEA})_2\text{PbI}_4$, respectively. Panels (A) show the inelastic neutron scattering spectra of $(\text{BA})_2\text{PbI}_4$ taken at 10 K and of $(\text{PEA})_2\text{PbI}_4$ taken at 8 K. Five different E_i settings were plotted to show the entire phonon spectra up to ~ 600 meV with appropriate energy resolutions. The phonon spectra we plotted for both samples are in the absolute units, barn/meV, via normalization to elastic incoherent scattering intensity (see details in Appendix. 2). Many nearly dispersion-less peaks are exhibited in the contour maps. They are well defined in energy which means the collective vibrational motions are coherent over space and time.

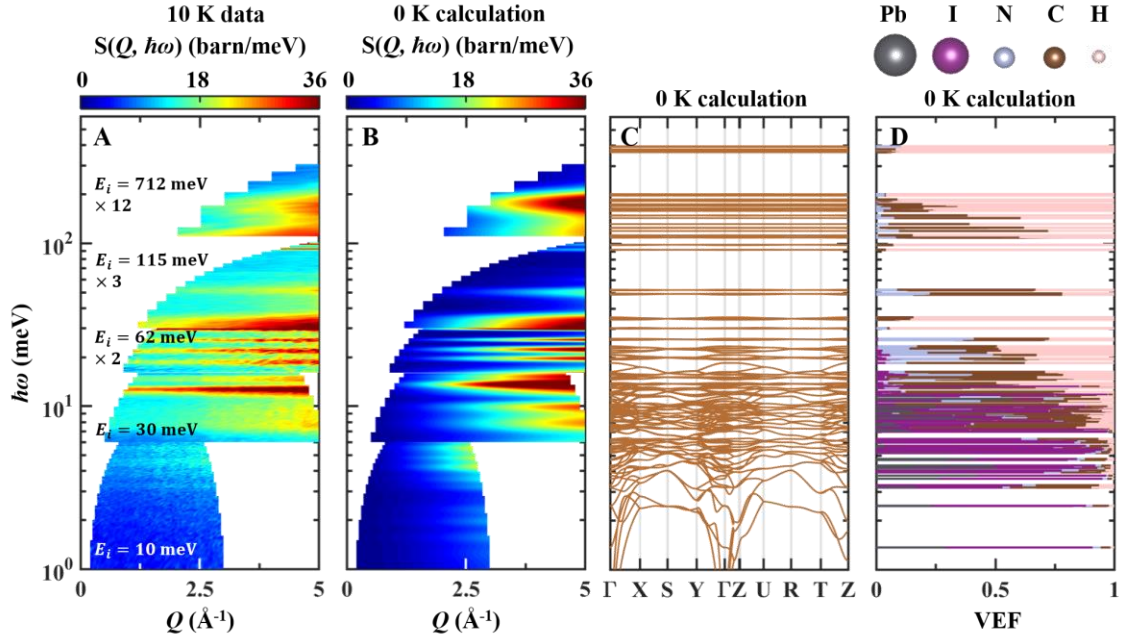


Fig. 16 Experimental phonon spectra and DFT calculations of $(\text{BA})_2\text{PbI}_4$.

(A) shows the experimental phonon spectra of $(\text{BA})_2\text{PbI}_4$ taken at 10 K with $E_i = 10, 30, 62, 115, 712$ meV. The intensities of $E_i = 62, 115,$ and 712 meV are rescaled by 2, 3, and 12 respectively. (B) shows the simulated phonon spectra using software OCLIMAX. (C) presents the calculated phonon band structure along high-symmetry reciprocal \mathbf{Q} points, $\Gamma = (0, 0, 0)$, $X = (\frac{1}{2}, 0, 0)$, $S = (\frac{1}{2}, \frac{1}{2}, 0)$, $Y = (0, \frac{1}{2}, 0)$, $Z = (0, 0, \frac{1}{2})$, $U = (\frac{1}{2}, 0, \frac{1}{2})$, $R = (\frac{1}{2}, \frac{1}{2}, \frac{1}{2})$, and $T = (0, \frac{1}{2}, \frac{1}{2})$. (D) contains the vibrational energy fractions at the Γ point for each phonon mode of $(\text{BA})_2\text{PbI}_4$. Here the gray, violet, cyan, brown, and pink spheres represent the energy fractions of Pb, I, N, C, and H atoms, respectively.

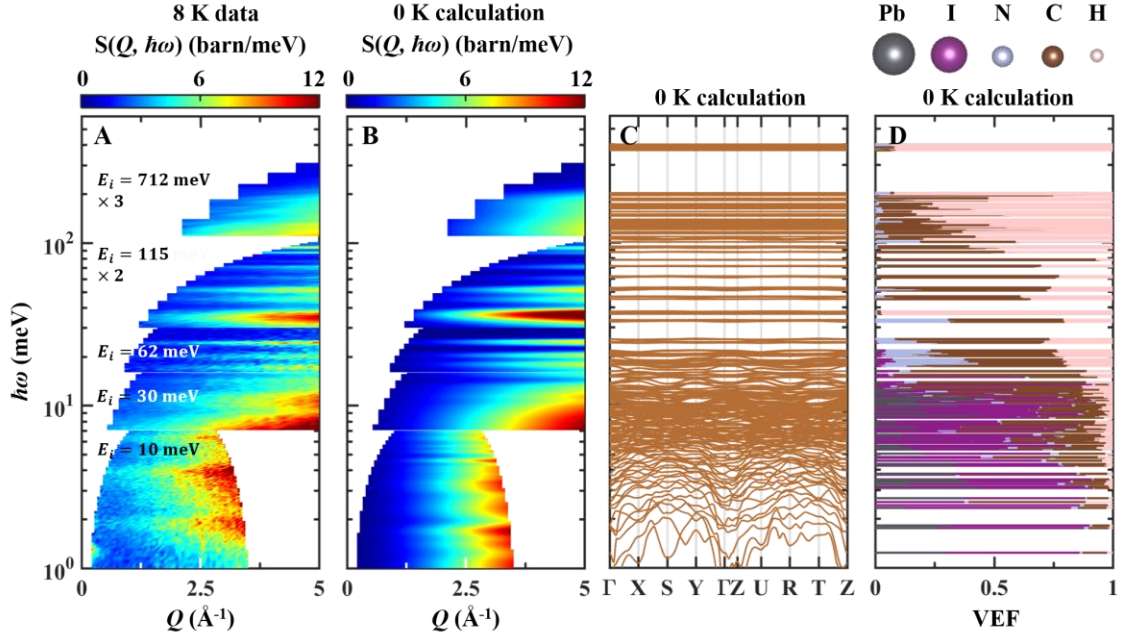


Fig. 17 Experimental phonon spectra and DFT calculations of $(\text{PEA})_2\text{PbI}_4$.

(A) shows the experimental phonon spectra of $(\text{PEA})_2\text{PbI}_4$ taken at 8 K with $E_i = 10, 30, 62, 115, 712$ meV. The intensities of $E_i = 115$ and 712 meV are rescaled by 2 and 3 respectively. (B) shows the simulated phonon spectra using software OCLIMAX. (C) presents the calculated phonon band structure along high-symmetry reciprocal \mathbf{Q} points, $\Gamma = (0, 0, 0)$, $X = (\frac{1}{2}, 0, 0)$, $S = (\frac{1}{2}, \frac{1}{2}, 0)$, $Y = (0, \frac{1}{2}, 0)$, $Z = (0, 0, \frac{1}{2})$, $U = (\frac{1}{2}, 0, \frac{1}{2})$, $R = (\frac{1}{2}, \frac{1}{2}, \frac{1}{2})$, and $T = (0, \frac{1}{2}, \frac{1}{2})$. (D) contains the vibrational energy fractions at the Γ point for each phonon mode of $(\text{PEA})_2\text{PbI}_4$. Here the gray, violet, cyan, brown, and pink spheres represent the energy fractions of Pb, I, N, C, and H atoms, respectively.

In order to identify the observed INS peaks, we have computed the atomic force constants based on the optimized low-temperature-phase crystal structure with the VASP package, and hence simulated the phonon spectra (Figs. 16, 17 panels (B)) using the software OCLIMAX and calculated phonon band (Figs. 16, 17 panels (C)) structures.

The simulation matches with the experimental data quite well which increases the reliability of the phonon identification.

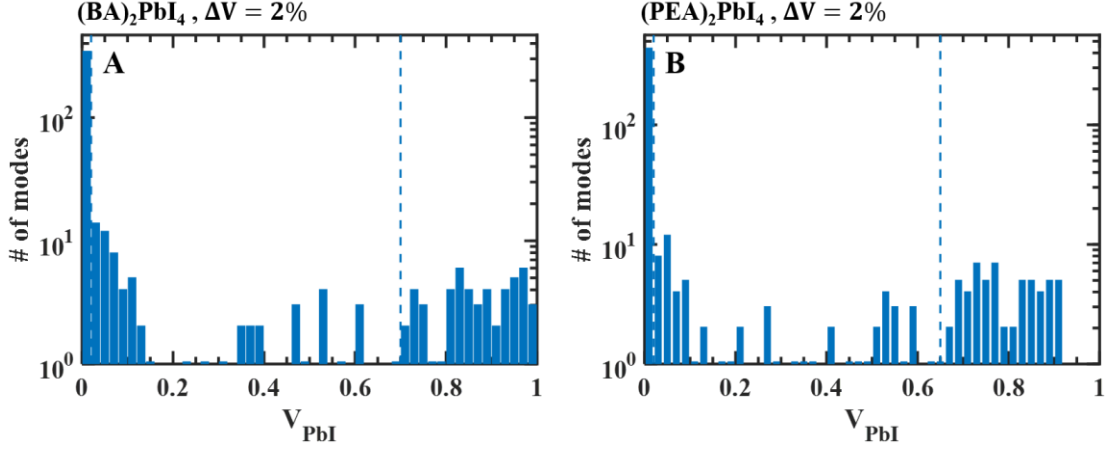


Fig. 18 Statistics of number of phonon modes with different Pb-I vibrational energy fractions for $(BA)_2PbI_4$ (A) and $(PEA)_2PbI_4$ (B).

The vertical bars represent the number of phonon modes with certain Pb-I energy fractions $[V_{PbI}, V_{PbI} + \Delta V]$. Vertical dash lines represent the threshold Pb-I energy fractions that separate the modes into inorganic modes ($V_{PbI} > 70\%$ for $(BA)_2PbI_4$ and 65% for $(PEA)_2PbI_4$), organic modes ($V_{PbI} < 2\%$), and hybrid modes.

We characterize the phonon modes into 3 different types: inorganic modes, hybrid modes, and organic modes in terms of the vibration energy fraction from different atoms (Figs. 16, 17 panels (D)). We take the summation of energy fractions of Pb and I as inorganic vibrational contribution V_{PbI} and summarize the number of phonon modes within certain energy fraction intervals $[V_{PbI}, V_{PbI} + \Delta V]$ (Fig. 18). The distribution of phonon modes as a function of Pb-I energy fractions shows predominant cut-off behaviors and indicates that the appropriate threshold percentage for inorganic modes which consists of mostly Pb-I vibrations is $\sim 70\%$ for $(BA)_2PbI_4$ and $\sim 65\%$ for

(PEA)₂PbI₄. To distinguish the organic modes where molecular vibrations make most (or all) contributions, the corresponding threshold percentage V_{PbI} is suggested to be $\sim 2\%$, below which the extremely large numbers of organic modes come into the statistics. The rest are hence identified as hybrid modes. Based on this characterization of phonon modes, we find that for both samples: most of the inorganic modes lie in the energy range of < 10 meV; the hybrid modes mostly locate in the energy range of 10~30 meV; and the energies of organic modes are usually in a few decades or hundreds of meVs.

3.3.2 Rotational dynamics

Before we move further, we emphasized that besides lattice vibrations, the rotation or reorientation of molecules in these materials may also make a difference. It has been experimentally shown that in 3D HOIPs, such as MAPbI₃, the reorientation of the polarized molecules can impose an efficient screening on the band-edge charge carriers, hence assist the polaron formation, and lead to the prolonged charge carrier lifetime [83]. Consequently, it is natural to expect that in 2D HOIPs the rotation or reorientation of organic molecules could also play a non-negligible role in the system's optoelectronic properties. Such relaxation process is experimentally manifested as diffusive signal from the elastic channel into the inelastic region. This rotational signal could merge with the low-energy acoustic and optical phonons of these materials (for example, the lowest energy of optical phonon modes at Γ point in (BA)₂PbI₄ is ~ 1.3 meV). Therefore, to distinguish the rotational and vibration contributions and properly identify phonons for both samples, we need to analyze the rotational dynamics of these materials.

To study the rotational dynamics of both samples, we performed temperature-dependent quasi-elastic neutron scattering (QENS) measurements at AMATERAS, J-PARC, with an incident neutron energy of 3.3 meV and resolution of 0.04 meV. We rescaled the data to elastic incoherent scattering intensity (see Appendix. 2) for direct comparison between the two samples. Fig. 19 selects QENS data at 5 temperatures for each sample. At ~ 180 K, the neutron scattering intensity concentrates in the elastic channel for both samples. As the temperature increases, the elastic channel intensity quickly diffuses into quasi-elastic region for $(\text{BA})_2\text{PbI}_4$, especially above 260 K (Fig. 19 (D)(E)). But for $(\text{PEA})_2\text{PbI}_4$, upon heating from 190 K to 310 K, only slight increments in quasi-elastic intensity ($|\hbar\omega| \leq 0.3$ meV) and enhancements of low-energy optical phonon intensity are observed. As mentioned in chapter 1, strong rotational relaxation or diffusion process would lead to high quasi-elastic neutron scattering intensity. The extremely different temperature-dependent behaviors QENS intensity of the two samples

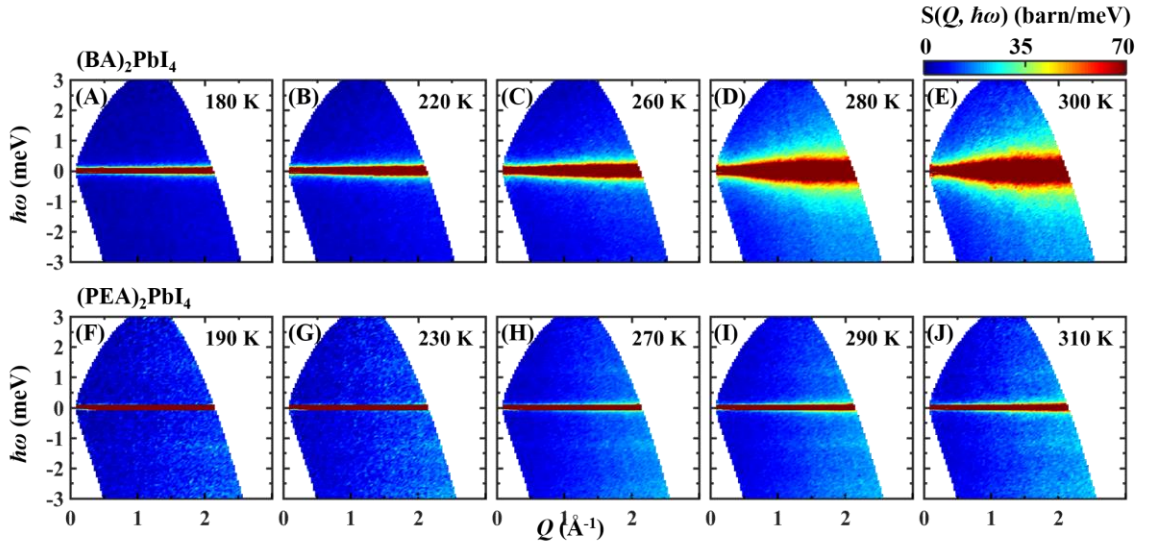


Fig. 19 Temperature-dependent quasi-elastic neutron scattering spectra of $(\text{BA})_2\text{PbI}_4$ (A-E) and $(\text{PEA})_2\text{PbI}_4$ (F-J) upon heating.

indicate that above 180 K, the rotational dynamics in $(\text{BA})_2\text{PbI}_4$ is much stronger than that in $(\text{PEA})_2\text{PbI}_4$ with similar external conditions.

In order to better understand the rotational motions of organic cations, we applied group theory analysis based on the local crystal symmetry and molecular symmetry, and fit the QENS data with the jump model [71]. We previously proposed [68] for $(\text{BA})_2\text{PbI}_4$ that the BA^+ cation possesses two types of jump rotational modes: the three-fold (C_3) modes of the terminal NH_3 , CH_3 groups which exist in both structural phases (phase transition at ~ 275 K); and the four-fold (C_4) mode of the entire BA^+ cation about the

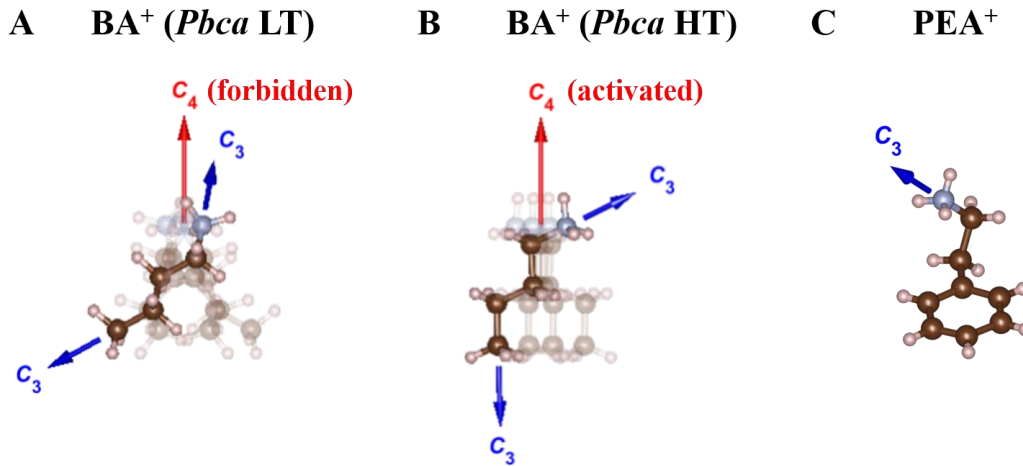


Fig. 20 Visualization of rotational modes in $(\text{BA})_2\text{PbI}_4$ and $(\text{PEA})_2\text{PbI}_4$.

(A)(B) show rotational modes of BA^+ in low-*T* phase (A) where the C_4 mode of the whole molecule about the crystallographic *c*-axis is forbidden, and in high-*T* phase (B) where the C_4 mode gets activated. (C) C_3 mode of NH_3 in $(\text{PEA})_2\text{PbI}_4$.

crystallographic *c*-axis which gets activated above the phase transition (Fig. 20 (A)(B)).

On the other hand, we found that in $(\text{PEA})_2\text{PbI}_4$, the C_3 mode of the NH_3 group alone can decently well explain the QENS data. The rotation of the benzene ring in PEA^+ cation is forbidden due to the tight stacking of molecules (Fig. 20 (C)).

Based on the rotational calculations introduced in section 3.2.2, we fit the QENS data with corresponding jump model (Fig. 21 and Fig. 22, see details in Appendix. 3). At low temperatures ($T < 275$ K), for both samples, the elastic signal shows a gradual decrease with increasing Q (panel (A)), yet the low energy quasi-elastic signals show a weak bump centered at $Q > 2 \text{ \AA}^{-1}$ (panel (B)(C)), which can be explained by the C_3 mode of NH_3 or CH_3 group. As the temperature reaches above 275 K, for $(\text{BA})_2\text{PbI}_4$, the

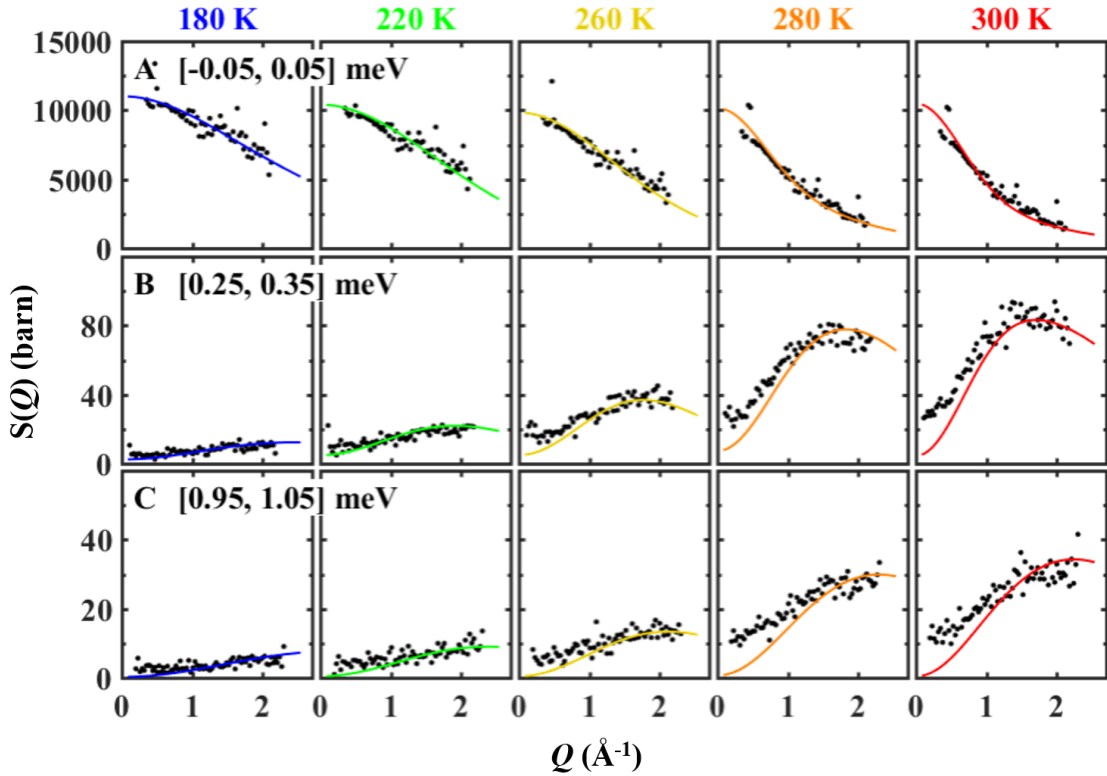


Fig. 21 Constant energy slices of QENS spectra and fittings of $(\text{BA})_2\text{PbI}_4$.

(A - C) the $\hbar\omega$ -integrated QENS data, $S(Q)$, over three different energy ranges, $-0.05 < \hbar\omega < 0.05$ meV (A), $0.25 < \hbar\omega < 0.35$ meV (B), $0.95 < \hbar\omega < 1.05$ meV (C), with five selected temperatures, 180 K, 220 K, 260 K (low-T *Pbca* orthorhombic phase), 280 K, 300 K (high-T *Pbca* orthorhombic phase). The black dots are the measured data, and the colored solid lines are the model fitted QENS intensity.

elastic signal decays much faster with the quasi-elastic signal showing a broad peak around 1.5 \AA^{-1} . This peculiar Q -dependence is captured by the appearance of the extra C_4 rotation of the whole BA^+ cation. Whereas for $(\text{PEA})_2\text{PbI}_4$, the data stays similar with that at low temperatures except for a bit faster decay of elastic signal due to the decrease in the Debye-Waller factor. See fitted parameters in Table. S5 of Appendix. 3.

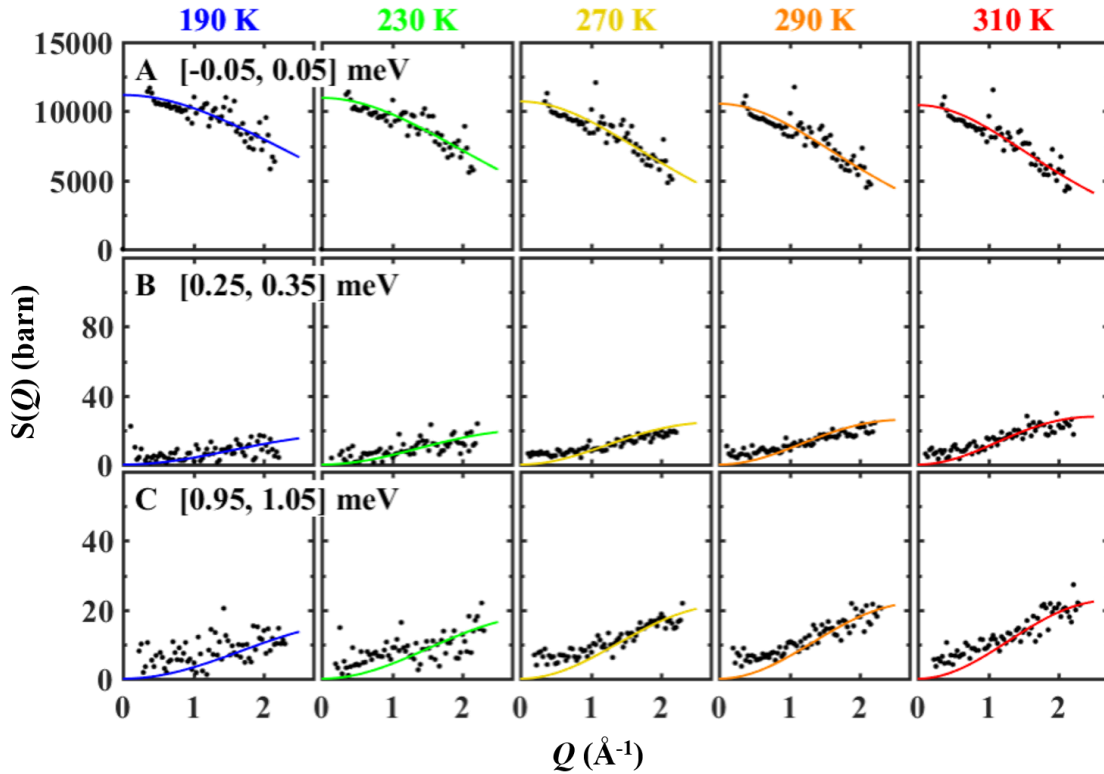


Fig. 22 Constant energy slices of QENS spectra and fittings of $(\text{PEA})_2\text{PbI}_4$.

(A - C) the $\hbar\omega$ -integrated QENS data, $S(Q)$, over three different energy ranges, $-0.05 < \hbar\omega < 0.05$ meV (A), $0.25 < \hbar\omega < 0.35$ meV (B), $0.95 < \hbar\omega < 1.05$ meV (C), with five selected temperatures, 190 K, 230 K, 270 K, 290 K, 310 K (triclinic $P-1$ single phase). The black dots are the measured data, and the colored solid lines are the model fitted QENS intensity.

3.3.3 Connections with optoelectronic properties

We separated the rotational and vibrational contributions from the measured phonon spectra based on the previous rotational dynamics analysis. Fig. 23 shows the temperature-dependent Q -integrated phonon spectra $S(\hbar\omega, T)$, with $E_i = 10$ and 30 meV, up to 23 meV which covers all of the inorganic modes and most of the hybrid modes. After the normalization into absolute units with respect to the elastic incoherent scattering intensity, the two datasets can be connected with each other decently well around 7 meV.

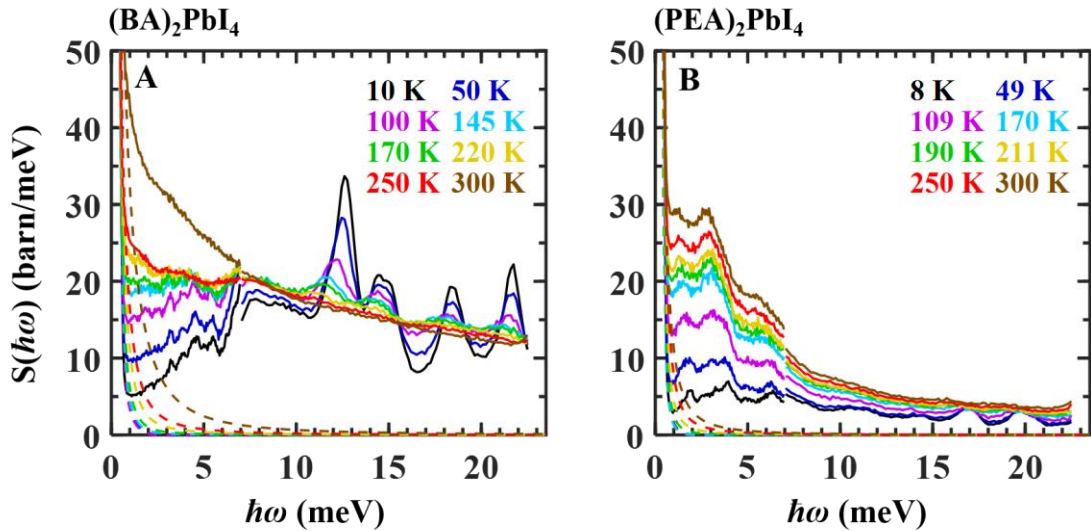


Fig. 23 Q -integrated phonon spectra of $(\text{BA})_2\text{PbI}_4$ (A) and $(\text{PEA})_2\text{PbI}_4$ (B) as a function of temperature.

Two datasets with $E_i = 10$ and 30 meV were connected at 7 meV after normalization into absolute units. The Q -integration range is selected as $1.0\sim 2.5 \text{ \AA}^{-1}$ which covers dominant phonon signal for both E_i s. The color dashed lines in the two panels are the estimated rotational contributions at corresponding temperatures as discussed in the main text.

Here, we emphasize that the high-energy organic modes describe the internal vibration of the organic molecules (stretching, tilting, twisting, etc.). They are less coupled to the external environment (excitons, free charges, ionic lattice, etc.) and hence are out of the discussion scope.

We applied the pure rotation term in the jump rotational model discussed in section 3.3.2 to the elastic incoherent scattering intensity of phonon spectra (see details in Appendix. 4) and estimated the rotation-related parameters (relaxation times and atomic displacements) via model fitting. The rotational contributions are hence determined as a function of temperature (color dashed lines in Fig. 23).

With the successful separation of rotational and vibrational contributions in our measured data, we try to find any possible relations that can link the structural dynamics to their optoelectronic properties. Fig. 24(B) shows the temperature dependent PLQY for $(\text{BA})_2\text{PbBr}_4$ and $(\text{PEA})_2\text{PbBr}_4$. Note that below ~ 150 K, the PLQYs of both bromides are similar and above 90%, and above 150 K, the PLQY of $(\text{BA})_2\text{PbBr}_4$ decreases much faster than that of $(\text{PEA})_2\text{PbBr}_4$ as the temperature increases (at room temperature $(\text{BA})_2\text{PbBr}_4$ only possesses a PLQY of $\sim 16\%$ while that of $(\text{PEA})_2\text{PbBr}_4$ is $\sim 70\%$). By performing DFT calculations and using Raman spectroscopy, Gong et al. [37] proposed that the higher crystal rigidity in $(\text{PEA})_2\text{PbBr}_4$ contributes to weaker electron-phonon coupling, less non-radiative recombination, and hence leads to higher PLQY at room temperature. Yet they did not explain the specific temperature dependences of PLQY in both samples. Based on our temperature-dependent neutron scattering data, we are able to examine the temperature-dependent connections between their structural dynamics and PLQY.

Fig. 24(A) shows the integrated phonon intensities of both samples after subtracting the rotational contributions. Two energy integration ranges are selected: 1.5~4.0 meV (mostly inorganic modes) and 12~16 meV (hybrid modes). We find that the inorganic phonon modes for both samples have similar intensities and temperature dependence (red hollow and solid circles in Fig. 24(A)). It is consistent with the fact that

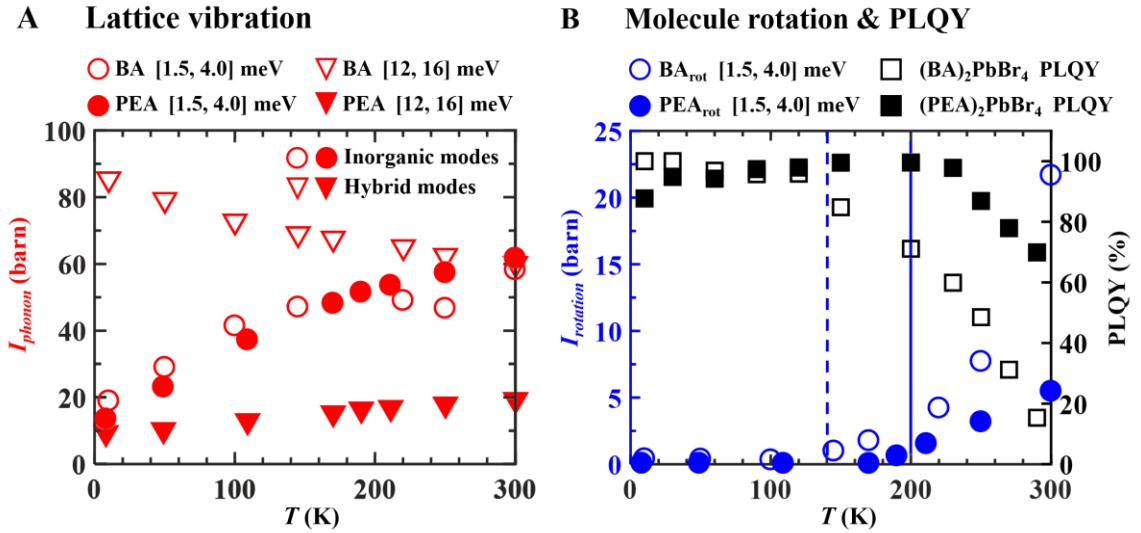


Fig. 24 Temperature-dependent phonon intensities, rotational contributions and PLQY of 2D MHPs.

(A) Temperature-dependent integrated phonon intensities of $(\text{BA})_2\text{PbI}_4$ and $(\text{PEA})_2\text{PbI}_4$ over certain energy ranges, $1.5 \leq \hbar\omega \leq 4.0$ meV (circles) and $12 \leq \hbar\omega \leq 16$ meV (triangles), and a Q range of $1 \sim 2.5 \text{ \AA}^{-1}$ after the subtraction of rotational contributions. (B) Blue circles show the rotational contributions of $(\text{BA})_2\text{PbI}_4$ and $(\text{PEA})_2\text{PbI}_4$ over the energy range of $1.5 \leq \hbar\omega \leq 4.0$ meV and same Q range. Blue dashed and solid lines represent the activation temperatures of rotational motions in $(\text{BA})_2\text{PbI}_4$ and $(\text{PEA})_2\text{PbI}_4$, respectively. Black squares represent the temperature-dependent PLQY of $(\text{BA})_2\text{PbBr}_4$ and $(\text{PEA})_2\text{PbBr}_4$ reported by Ref. [37].

regardless of different organic configurations, the inorganic networks (Pb-I) of both layered-structure samples are similar, leading to similar vibrational response of inorganic modes, which consist of mostly the vibration of Pb-I sublattice, to the incident neutrons. On the other hand, the scattering intensities of hybrid modes (red hollow and solid triangles) are quite different for the two samples. The much lower intensities of hybrid modes in $(\text{PEA})_2\text{PbI}_4$ than in $(\text{BA})_2\text{PbI}_4$ suggests that the tight stacking of PEA^+ cations probably restrict their vibrational degrees of freedom and hence suppresses the vibrational response of hybrid modes, where organic cation vibrations are coupled with the inorganic Pb-I network vibrations, to the incident neutrons. Nevertheless, the temperature dependence of either inorganic phonon modes or hybrid phonon modes does not show predominant correlations with the PLQY of their bromide counterparts (Fig. 24(B)).

In contrast with the vibrational dynamics, the estimated rotational contributions exhibit almost one-to-one correspondence to the PLQY indicated by their bromide equivalents that we assume to be similar with or same as the iodides (Fig. 24 (B)). Below ~ 150 K, the rotational motions of organic molecules in both samples are almost frozen manifested by the extremely weak rotational intensities. In the same temperature range, the bromide counterparts of both samples show similar and high PLQY ($> 90\%$). Upon heating above the activation temperatures (blue dashed and solid lines in Fig. 24 (B): ~ 150 K for $(\text{BA})_2\text{PbI}_4$, and ~ 200 K for $(\text{PEA})_2\text{PbI}_4$), the rotational dynamics get activated and the rotational intensity increases much faster in $(\text{BA})_2\text{PbI}_4$ than in $(\text{PEA})_2\text{PbI}_4$, coinciding with the faster reduction of PLQY observed in $(\text{BA})_2\text{PbBr}_4$. The activation temperatures are consistent with those at which the PLQY of the two bromides start to

decrease. This coincidence in the temperature dependence strongly indicates that the rotational dynamics of organic molecules in 2D MHPs plays a dominant role in their PLQY. We postulated a scenario for the detailed mechanism that in $(\text{BA})_2\text{PbI}_4$ the much drastic rotational motions of charged organic molecules could interrupt the binding energy potential around the stable excitons, lower the energy barrier that the stable exciton takes to decompose into free charge carriers which fortifies exciton fissions and exposes charge carriers to more non-radiative scatterings from the environment (such as phonons), and hence suppresses the PLQY.

Chapter 4

Summary

In this thesis, we reported our neutron scattering studies on a strongly correlated magnetic system, $\text{Sr}_2\text{CuTe}_{0.5}\text{W}_{0.5}\text{O}_6$, and two weakly correlated non-magnetic systems, $(\text{BA})_2\text{PbI}_4$ (butylammonium lead iodide) and $(\text{PEA})_2\text{PbI}_4$ (phenethyl-ammonium lead iodide).

For $\text{Sr}_2\text{CuTe}_{0.5}\text{W}_{0.5}\text{O}_6$, using the sub-K temperature and 20 μeV energy resolution neutron scattering experiments we show that the system transits from a gapless disorder-induced spin liquid to a new quantum state below $T_f \sim 1.7(1)$ K with an extremely weak frozen moment of $\langle S \rangle / S \sim 0.1$. The asymmetric momentum (Q) dependence of the low energy spin fluctuations and linearity of its dynamic susceptibility $\chi''(\hbar\omega)$ with $\hbar\omega$ for $\hbar\omega < k_B T_f$ confirms the two-dimensionality of the system which is consistent with a Halperin-Saslow excitations. The phenomenological fitting to the Q -dependence of low energy spin fluctuations reveals the short-range dynamical correlations with an in-plane correlation length of $\xi \sim \sqrt{2} d_{NN}$, where d_{NN} is the distance between the nearest neighbor spins. It is surprising to observe the extremely weak freezing in this highly fluctuating quantum regime which presents great theoretical challenges to fully understand its different magnetic phases.

For the two non-magnetic weakly correlated systems, $(\text{BA})_2\text{PbI}_4$ and $(\text{PEA})_2\text{PbI}_4$, we characterized their rotational and vibrational dynamics by using time-of-flight neutron scattering experimental techniques, and theoretical tools such as group theory analysis and density-functional-theory calculations. In $(\text{BA})_2\text{PbI}_4$, two types of rotational modes

were revealed: the three-fold (C_3) rotational modes of NH_3 and CH_3 groups; and the four-fold (C_4) rotational mode of the entire molecule about the crystallographic c -axis, which only gets activated in its high-temperature structural phase ($T > 275$ K). Whereas in $(PEA)_2PbI_4$, only the C_3 rotational of the NH_3 group was identified.

Based on the characterized rotational dynamics of both samples, we extracted the rotational contributions from the measured neutron scattering spectra. We find that the vibrational dynamics of both samples do not show predominant correlations with the PLQY indicated by their bromide equivalents that we assume to be similar with or same as the iodides. On the other hand, the rotational dynamics exhibits a surprising correspondence to PLQY that: below ~ 150 K when the rotational dynamics of both samples are frozen, the PLQY of their bromide equivalents stay at high levels ($> 90\%$); while above 150 K, the rotational motion of organic molecules in $(BA)_2PbI_4$ get enhanced much faster than that in $(PEA)_2PbI_4$, which coincides with the faster decay of PLQY observed in $(BA)_2PbBr_4$. The excellent correspondence suggests that it is the rotational dynamics of organic molecules in 2D MHPs that dominate the optoelectronic performance such as PLQY.

Appendix 1.

Magnetic Scattering Experimental Details

This appendix shows the magnetic sum rule and method of normalizing magnetic scattering intensity in absolute units according to nuclear Bragg peak intensity. The temperature-independent background determination method and the details of the phenomenological $S(Q)$ model fittings are also listed.

1. Temperature independent background determination algorithm

To avoid confusion, we use $I(Q, \hbar\omega, T)$ to denote the raw measured data, $bkg(Q, \hbar\omega)$ as the temperature-independent background, and $S(Q, \hbar\omega, T)$ as the magnetic intensity we evaluate. The core formalism in this algorithm is to apply the detailed balance condition on $S(Q, \hbar\omega, T)$:

$$\begin{aligned} I(Q, \hbar\omega, T) &= bkg(Q, \hbar\omega) + S(Q, \hbar\omega, T) \\ I(Q, -\hbar\omega, T) &= bkg(Q, -\hbar\omega) + S(Q, \hbar\omega, T)e^{-\hbar\omega/k_B T} \end{aligned} \tag{Eq. 18}$$

Since the detailed balance condition of the powder averaged data does not depend on momentum (Q), we slice the data into many Q cuts and focus on the $\hbar\omega$ dependence of each cut. Choose appropriate binning size of $\hbar\omega$ to get symmetric spectrum ($\hbar\omega_{max} = \hbar|\omega_{min}|$). For each Q cut, assuming the sliced data consists of $I(\hbar\omega, T)$, $bkg(\hbar\omega)$, and $S(\hbar\omega, T)$. Then we set up the deviation function for each $\hbar\omega$

$$\begin{aligned}
Dev(\hbar\omega) = & \sum_i \frac{(I(\hbar\omega, T_i) - bkg(\hbar\omega) - S(\hbar\omega, T_i))^2}{\sigma^2(\hbar\omega, T_i)} \\
& + \sum_i \frac{(I(-\hbar\omega, T_i) - bkg(-\hbar\omega) - e^{-\hbar\omega/k_B T_i} S(\hbar\omega, T_i))^2}{\sigma^2(-\hbar\omega, T_i)}
\end{aligned}
\tag{Eq. 19}$$

where T_i is the temperature of the dataset. $\sigma(\hbar\omega, T_i)$ is the data error bar at $\hbar\omega$ in corresponding Q cut of the corresponding temperatures. The optimized results will give the minimum of this deviation function. Thus, we take the partial derivative with respect to each unknown variable:

$$\frac{\partial Dev}{\partial bkg(\hbar\omega)} = 0, \quad \frac{\partial Dev}{\partial bkg(-\hbar\omega)} = 0, \quad \frac{\partial Dev}{\partial S(\hbar\omega, T_i)} = 0
\tag{Eq. 20}$$

Consequently, we will get $n+2$ equations involving the $n+2$ unknown variables (assume we have unknown variables: $bkg(\hbar\omega)$, $bkg(-\hbar\omega)$, $S(\hbar\omega, T_i)$, $i = 1, 2, \dots, n$). Make the determinant of the coefficient matrix of these equations to be 0, we can get the optimized results that follow the detailed balance condition, $S_{optimized}(\hbar\omega > 0)$, and the temperature-independent background $bkg(\pm\hbar\omega)$. Apply this algorithm to each Q cut, we finally obtain the background-subtracted magnetic intensity $S_{bkg-subtracted}(Q, \hbar\omega > 0)$. Note that in time-of-flight experiments, the resolution window in general may deviate from the detailed balance condition due to the instrument limitations, thus this algorithm works well down to the instrument resolution limit ($|\hbar\omega| \geq E_{res}$).

2. Sum rule for the dynamic spin structure factor

For a system of identical magnetic atoms with spin S , the magnetic scattering cross-section is described by

$$\frac{d^2\sigma(\mathbf{Q}, \hbar\omega)}{d\Omega d(\hbar\omega)} = N \frac{k_f}{k_i} (\gamma r_0)^2 f^2(\mathbf{Q}) \sum_{\alpha, \beta} \frac{g_\alpha g_\beta}{2} (\delta_{\alpha\beta} - \hat{Q}_\alpha \hat{Q}_\beta) S^{\alpha\beta}(\mathbf{Q}, \hbar\omega)$$

(Eq. 21)

$S^{\alpha\beta}(\mathbf{Q}, \hbar\omega)$ is called the dynamical spin structure factor,

$$S^{\alpha\beta}(\mathbf{Q}, \hbar\omega) = \int_{-\infty}^{\infty} e^{-i\omega t} \frac{1}{N} \sum_{j, j'} \langle e^{-i\mathbf{Q}\cdot(\mathbf{R}_j - \mathbf{R}_{j'})} S_j^\alpha(0) S_{j'}^\beta(t) \rangle \frac{dt}{2\pi\hbar}$$

(Eq. 22)

The above results refer to the ideal rigid lattice, and do not account for the lattice's thermal vibrations or the structural disorder. These effects can be accounted for by multiplying the magnetic cross-section with the Debye-Waller factor, $e^{-2W(\mathbf{Q})}$.

To evaluate the sum rule of the dynamic spin structure factor, we first integrate $S^{\alpha\beta}(\mathbf{Q}, \hbar\omega)$ over the entire energy range,

$$\begin{aligned} S^{\alpha\beta}(\mathbf{Q}) &\equiv \int_{-\infty}^{\infty} S^{\alpha\beta}(\mathbf{Q}, \hbar\omega) d(\hbar\omega) \\ &= \int_{-\infty}^{\infty} d(\hbar\omega) \int_{-\infty}^{\infty} e^{-i\omega t} \frac{1}{N} \sum_{j, j'} \langle e^{-i\mathbf{Q}\cdot(\mathbf{R}_j - \mathbf{R}_{j'})} S_j^\alpha(0) S_{j'}^\beta(t) \rangle \frac{dt}{2\pi\hbar} \end{aligned}$$

(Eq. 23)

In the double integral (Eq. 23), we first do the $\hbar\omega$ integral,

$$\frac{1}{2\pi\hbar} \int_{-\infty}^{\infty} e^{-i\omega t} d(\hbar\omega) = \delta(t)$$

(Eq. 24)

then, we evaluate the time integral,

$$S^{\alpha\beta}(\mathbf{Q}) = \frac{1}{N} \sum_{j,j'} \langle e^{-i\mathbf{Q}\cdot(\mathbf{R}_j - \mathbf{R}_{j'})} S_j^\alpha(0) S_{j'}^\beta(0) \rangle = \frac{1}{N} \langle S_{\mathbf{Q}}^\alpha S_{-\mathbf{Q}}^\beta \rangle$$

(Eq. 25)

where $S_{\mathbf{Q}}^\alpha = \sum_j e^{-i\mathbf{Q}\cdot\mathbf{R}_j} S_j^\alpha$ is the lattice Fourier transformation of the lattice spin operators. Integrating Eq. 25 over the 1st Brillouin zone and taking the trace over the spin indices, $\alpha = \beta$, yields the sum rule,

$$\begin{aligned} \sum_{\alpha} \frac{\int S^{\alpha\alpha}(\mathbf{Q}) d^3\mathbf{Q}_{BZ}}{\int d^3\mathbf{Q}_{BZ}} &= \sum_{\alpha} \frac{1}{N} \int \langle S_{\mathbf{Q}}^\alpha S_{-\mathbf{Q}}^\alpha \rangle \frac{V_0}{(2\pi)^3} d^3\mathbf{Q} = \frac{1}{N} \sum_{j,\alpha} \langle (S_j^\alpha)^2 \rangle \\ &= \sum_{\alpha} \langle (S^\alpha)^2 \rangle = \langle \mathbf{S}^2 \rangle = S(S+1) \end{aligned}$$

(Eq. 26)

Here V_0 is the volume of the crystal unit cell.

In summary, the sum rule for the integral spectral weight of $S^{\alpha\beta}(\mathbf{Q}, \hbar\omega)$ is

$$\sum_{\alpha} \int \int_{-\infty}^{\infty} S^{\alpha\alpha}(\mathbf{Q}, \hbar\omega) \frac{V_0}{(2\pi)^3} d^3\mathbf{Q}_{BZ} d(\hbar\omega) = S(S+1)$$

(Eq. 27)

In our case, the total spectra weight is evaluated to be $\frac{2}{3}S(S + 1)$ as discussed in session 3 below.

3. Normalization

Magnetic neutron scattering cross-section from a powder sample with a single species of magnetic atoms can be written as [39, 41]

$$\frac{d^2\sigma}{d\Omega d(\hbar\omega)} = N \frac{k_f}{k_i} (\gamma r_0)^2 \left\{ \frac{1}{2} g f(Q) \right\}^2 e^{-2W} \tilde{S}(Q, \hbar\omega) \quad (\text{Eq. 28})$$

where $\tilde{S}(Q, \hbar\omega) = \int \frac{d\Omega}{4\pi} \sum_{\alpha, \beta} (\delta_{\alpha, \beta} - \hat{Q}_\alpha \hat{Q}_\beta) S^{\alpha\beta}(\mathbf{Q}, \hbar\omega)$, $\frac{\gamma r_0}{2} = 0.2695 \times 10^{-12}$ cm, $g \approx 2$, e^{-2W} is the Debye-Waller factor, and $f(Q)$ is the magnetic form factor. Here $S^{\alpha\beta}(\mathbf{Q}, \hbar\omega)$ is the dynamic spin structure factor in section 2.

After the monitor normalization and $\frac{k_f}{k_i}$ modification in time-of-flight spectrometer, the reduced neutron scattering intensity becomes

$$I(\mathbf{Q}, \hbar\omega) = \int_{-\infty}^{\infty} d(\hbar\omega_0) \int dQ_0 N (\gamma r_0)^2 \left\{ \frac{1}{2} g f(Q) \right\}^2 e^{-2W} \tilde{S}(Q, \hbar\omega) R(Q_0, \hbar\omega_0, Q, \hbar\omega) \quad (\text{Eq. 29})$$

where $R(Q_0, \hbar\omega_0, Q, \hbar\omega)$ is the instrument resolution function. With the assumption that $\tilde{S}(Q, \hbar\omega)$ is relatively smooth and the resolution function varies much more rapidly in the

region of interest, we can make the necessary approximation to decouple the resolution function and $\tilde{S}(Q, \hbar\omega)$,

$$I(\mathbf{Q}, \hbar\omega) = N(\gamma r_0)^2 \left\{ \frac{1}{2} gf(Q) \right\}^2 e^{-2W} \tilde{S}(Q, \hbar\omega) R_0$$

(Eq. 30)

where $R_0 = \int_{-\infty}^{\infty} d(\hbar\omega_0) \int dQ_0 R(Q_0, \hbar\omega_0, Q, \hbar\omega)$ is the resolution volume, which would be only instrument – dependent.

After putting all things together, we finally obtain

$$\tilde{S}(Q, \hbar\omega) = \frac{I(\mathbf{Q}, \hbar\omega)}{(\gamma r_0)^2 \left\{ \frac{1}{2} gf(Q) \right\}^2 e^{-2W} NR_0}$$

(Eq. 31)

Here $\tilde{S}(Q, \hbar\omega)$ has a unit of meV^{-1} or eV^{-1} . In the case of multiple magnetic atoms in one crystal unit cell, we need to divide $\tilde{S}(Q, \hbar\omega)$ by the number of magnetic atoms, N_m .

In most cases, $\tilde{S}(Q, \hbar\omega)$ discussed above is the normalized magnetic spectra with absolute units that people correspond to. In order to normalize the magnetic spectra, we still need the product of the resolution volume and the number of unit cells, NR_0 . It can be calculated using the nuclear Bragg peaks.

The nuclear Bragg scattering cross section is

$$\frac{d^2\sigma}{d\Omega d(\hbar\omega)} = N \frac{(2\pi)^3}{V_0} \sum_{\boldsymbol{\tau}} \delta^3(\mathbf{Q} - \boldsymbol{\tau}) |F_N(\boldsymbol{\tau})|^2 \delta(\hbar\omega)$$

(Eq. 32)

where V_0 is the volume of the crystal unit cell, $\boldsymbol{\tau}$ is the nuclear Bragg peak position, and $F_N(\boldsymbol{\tau})$ is the nuclear structure factor of Bragg peak $\boldsymbol{\tau}$.

When the sample is powder,

$$\frac{d^2\sigma}{d\Omega d(\hbar\omega)} = N \frac{(2\pi)^3}{V_0} \sum_{\boldsymbol{\tau}} \frac{\delta(Q - \tau)}{4\pi\tau^2} n_{\boldsymbol{\tau}} |F_N(\boldsymbol{\tau})|^2 \delta(\hbar\omega)$$

(Eq. 33)

where $n_{\boldsymbol{\tau}}$ is the multiplicity of Bragg peaks with $\boldsymbol{\tau}$. The monitor-normalized intensity of the Bragg peak around τ is

$$\begin{aligned} I_N(Q, \hbar\omega) &= \int dQ_0 \int d(\hbar\omega_0) N \frac{(2\pi)^3}{V_0} \frac{\delta(Q_0 - \tau)}{4\pi\tau^2} n_{\boldsymbol{\tau}} |F_N(\boldsymbol{\tau})|^2 \delta(\hbar\omega_0) R(Q_0, Q, \hbar\omega_0, \hbar\omega) \\ &= N \frac{(2\pi)^3}{V_0} \frac{n_{\boldsymbol{\tau}}}{4\pi\tau^2} |F_N(\boldsymbol{\tau})|^2 R(Q - \tau, \hbar\omega) \end{aligned}$$

(Eq. 34)

where $R(Q_0, Q, \hbar\omega_0, \hbar\omega)$ is the instrument resolution function. Integrating I_N over both the energy transfer and momentum transfer with the approximation that $R(Q - \tau)$ does not depend on τ , we obtain

$$\begin{aligned} &\int_{Q_1}^{Q_2} dQ \int_{-\infty}^{\infty} d(\hbar\omega) I_N(Q, \hbar\omega) \\ &= N \int_{Q_1}^{Q_2} dQ \int_{-\infty}^{\infty} d(\hbar\omega) R(Q, \hbar\omega) \sum_{Q_1 < \tau < Q_2} \frac{(2\pi)^3}{V_0} \frac{n_{\boldsymbol{\tau}}}{4\pi\tau^2} |F_N(\boldsymbol{\tau})|^2 \end{aligned}$$

(Eq. 35)

In that the momentum resolution is much smaller than the momentum integration range,

we can make the approximation $\int_{Q_1}^{Q_2} R(Q, \hbar\omega) dQ \approx \int_{-\infty}^{\infty} R(Q, \hbar\omega) dQ$. Then

$$NR_0 = N \int_{Q_1}^{Q_2} dQ \int_{-\infty}^{\infty} d(\hbar\omega) R(Q, \hbar\omega) = \frac{\int_{Q_1}^{Q_2} dQ \int_{-\infty}^{\infty} d(\hbar\omega) I_N(Q, \hbar\omega)}{\sum_{Q_1 < \tau < Q_2} \frac{(2\pi)^3}{V_0} \frac{n_\tau}{4\pi\tau^2} |F_N(\boldsymbol{\tau})|^2}$$

(Eq. 36)

Using the normalization constant, NR_0 , we can transfer the raw data into absolute units.

In our paper, when we discuss the Q dependence or energy dependence of the data in absolute units, we refer to $S(Q, \hbar\omega) = f^2(Q) \tilde{S}(Q, \hbar\omega)$. When we evaluate the spectral weight or frozen spin degrees, we calculate $\tilde{S}(Q, \hbar\omega)$ related values.

In the isotropic fluctuation case (our case), $\tilde{S}(Q, \hbar\omega) = 2S^{xx}(Q, \hbar\omega) = 2S^{yy}(Q, \hbar\omega) = 2S^{zz}(Q, \hbar\omega)$. Due to the orientation isotropy, we have

$$\frac{\int_{BZ} dQ \int S^{xx}(Q, \hbar\omega) d(\hbar\omega)}{\int_{BZ} dQ} = \frac{1}{3} S(S+1), \text{ thus the total spectra weight of our data is}$$

$$\frac{\int_{BZ} dQ \int \tilde{S}(Q, \hbar\omega) d(\hbar\omega)}{\int_{BZ} dQ} = \frac{2}{3} S(S+1).$$

4. $S(Q)$ model fitting

We use the lattice-Lorentzian functions to fit the Q -dependence of low-energy spin fluctuations. The fitted parameters are the correlation lengths along three principal axes. Due to the two-dimensional features and tetragonal structural symmetry of the system, we presume $\xi_{out-of-plane} \rightarrow 0$ and $\xi_x = \xi_y = \xi_{in-plane} = \xi$. One thing that needs clarifications is that the ‘plane’ in the term ‘in-plane’ here refers to the x - y plane

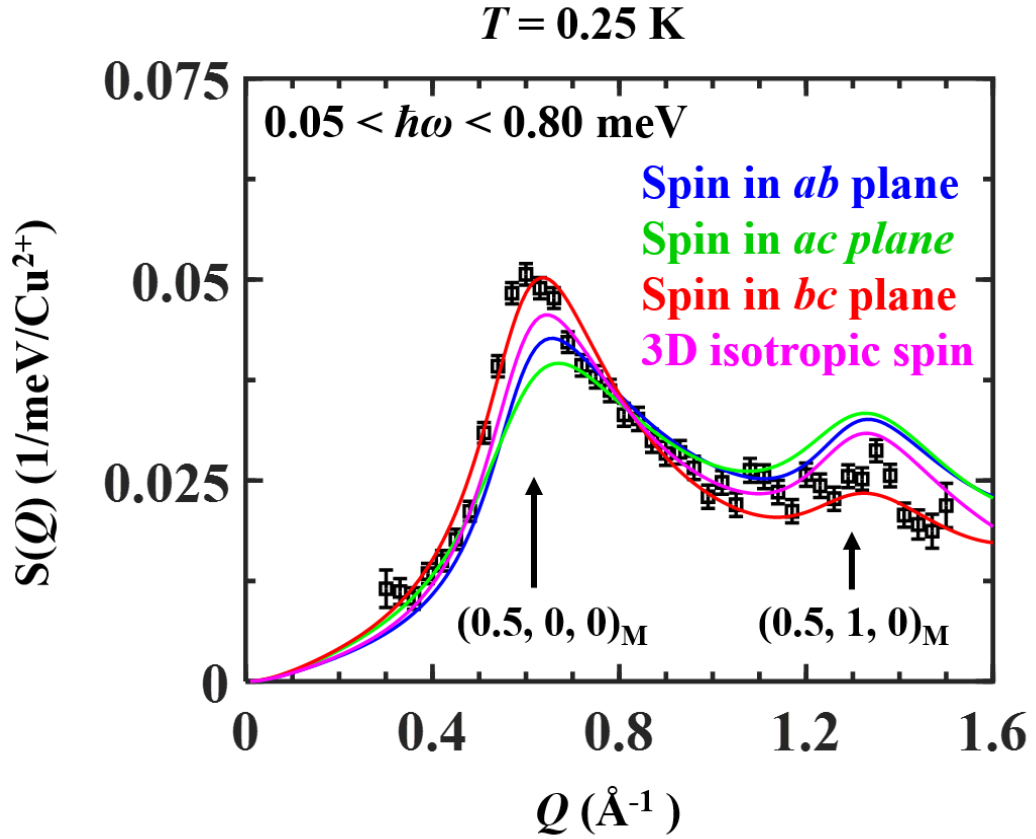


Fig. 25 Phenomenological $S(Q)$ fittings of low-energy spin fluctuations of $\text{Sr}_2\text{CuTe}_{0.5}\text{W}_{0.5}\text{O}_6$.

$S(Q)$ fittings with different spin configurations are plotted: spin in ab plane (blue), spin in bc plane (green), spin in ac plane (red), and 3D isotropic spins (pink).

($J_1 - J_2$ plane) of the tetragonal crystal structure. It is different from the plane involved in the spin orientation discussion next.

In the function, we use $\mathbf{q}_m = \left(\frac{1}{2}, 0, 0\right)$ and $\left(\frac{1}{2}, 1, 0\right)$. Note that we are trying to fit a $S(Q)$ spectrum with respect to scalar Q while the phenomenological model is a function of vector \mathbf{Q} . Thus, powder averaging is necessary. The proposed function is convoluted with the instrumental resolution after powder averaging. Meanwhile, the magnetic structure factor, $|F_m^\perp(\mathbf{Q})|^2$, contains the spin orientations implicitly, which calls for different trials of spin orientations in the model fitting. No static long-range order was observed in the system at low temperatures, indicating the random orientations of the magnetic spins. Here, to interpret the antiferromagnetic wave vector $\mathbf{q}_m = \left(\frac{1}{2}, 0, 0\right)$, we construct antiferromagnetic spin arrays along a -direction (one of the square-lattice axes). The trial configurations (Fig. 25) we used to interpret the random spin orientations include: 2D isotropic spin orientations in ab plane, in ac plane, in bc plane, and 3D isotropic spin orientations, among which the configuration that spins lie in bc plane with 2D isotropic orientations gives the best fit. The correlation length ξ was extracted from the fitting using this spin configuration. Note that bc plane is perpendicular to the wave vector which suggests the dominant transverse contributions in the low-energy spin fluctuations.

Appendix 2.

Normalization to elastic incoherent scattering intensity

Both samples contain lots of hydrogen atoms, which makes it more straightforward and easier to normalize the intensity into absolute units using the elastic incoherent scattering intensities. The cross section for elastic incoherent scattering is quite simple:

$$\left(\frac{d\sigma}{d\Omega}\right)_{inc}^{el} = \frac{N}{4\pi} \sum_j \sigma_j^{inc} e^{-2W}$$

(Eq. 37)

where σ_j^{inc} is the incoherent neutron scattering cross section of the j -th atom. Based on Eq. 37, the energy integrated elastic incoherent scattering intensity

$$I_{inc}^{el}(Q) = \int_{-E_{res}}^{+E_{res}} I(Q, \hbar\omega) d(\hbar\omega) = \frac{N}{4\pi} \sum_j \sigma_j^{inc} e^{-2W} R_0$$

(Eq. 38)

where R_0 is the resolution volume mentioned in the Appendix 1. Thus, by fitting the base-temperature energy integrated elastic incoherent scattering intensity $I_{inc}^{el}(Q)$ to the theoretical model $A \cdot \sum_j \sigma_j^{inc} e^{-2W}$, where $e^{-2W} = e^{-(u^2)Q^2}$, we can extract the normalization constant

$$NR_0 = 4\pi \cdot A = \frac{I_{inc}^{el}(Q)}{\sum_j \sigma_j^{inc} e^{-2W}}$$

(Eq. 39)

Appendix 3.

Jump Model Details

This appendix shows the details of the jump model analysis of (BA)₂PbI₄ and (PEA)₂PbI₄.

The rotational dynamics of (BA)₂PbI₄ was discussed in details in Ref. 68. Here we repeat it for reading convenience. Two intrinsic rotational modes are revealed in (BA)₂PbI₄: C₃ and C₄ modes. Table S1 shows the character tables for point group C₃ and C₄. The NH₃ and CH₃ groups experience rotational mode $\Gamma = C_4 \otimes C_3$ and the rest of CH₂ groups experience $\Gamma = C_4$ only. Based on direct product rules in group theory and equivalent atomic position distributions (Fig. 26), we can calculate the corresponding τ_γ and $A_\gamma(Q)$ for them (Table S2, S3).

Table. S1 Character tables for C₃ and C₄.

The point group C₃ has two irreducible representations: one one-dimensional representation A, and one two-dimensional representation E. The point group C₄ has three irreducible representations: two one-dimensional representations A and B, and one two-dimensional representation E.

C ₃ group	E	2C ₃
A	1	1
E	2	-1

C_4 group	E	$2C_4$	C_2
A	1	1	1
B	1	-1	1
E	2	0	-2

Table. S2 Model details for jump mode $\Gamma = C_4 \otimes C_3$.

Γ_γ	$\frac{1}{\tau_\gamma}$	$36 \cdot A_\gamma(Q)$
$A \otimes A$	0	$3 + 6j_1 + 2j_2 + 2j_3 + 2j_4 + j_5 + 2j_6 + 2j_7 + 2j_8 + 2j_9$ $+ 2j_{10} + 2j_{11} + j_{12} + 2j_{13} + 2j_{14} + 2j_{15} + j_{16}$
$A \otimes E$	$\frac{3}{\tau_{C_3}}$	$6 - 6j_1 + 4j_2 - 2j_3 - 2j_4 + 2j_5 - 2j_6 - 2j_7 - 2j_8 - 2j_9$ $+ 4j_{10} - 2j_{11} + 2j_{12} - 2j_{13} - 2j_{14} + 4j_{15} + 2j_{16}$
$B \otimes A$	$\frac{4}{\tau_{C_4}}$	$3 + 6j_1 - 2j_2 - 2j_3 - 2j_4 + j_5 + 2j_6 + 2j_7 - 2j_8 - 2j_9$ $- 2j_{10} - 2j_{11} + j_{12} + 2j_{13} - 2j_{14} - 2j_{15} + j_{16}$
$B \otimes E$	$\frac{4}{\tau_{C_4}} + \frac{3}{\tau_{C_3}}$	$6 - 6j_1 - 4j_2 + 2j_3 + 2j_4 + 2j_5 - 2j_6 - 2j_7 + 2j_8 + 2j_9$ $- 4j_{10} + 2j_{11} + 2j_{12} - 2j_{13} + 2j_{14} - 4j_{15} + 2j_{16}$
$E \otimes A$	$\frac{2}{\tau_{C_4}}$	$6 + 12j_1 - 2j_5 - 4j_6 - 4j_7 - 2j_{12} - 4j_{13} - 2j_{16}$
$E \otimes E$	$\frac{2}{\tau_{C_4}} + \frac{3}{\tau_{C_3}}$	$12 - 12j_1 - 4j_5 + 4j_6 + 4j_7 - 4j_{12} + 4j_{13} - 4j_{16}$

Here j_i represent the zeroth spherical Bessel function $j_0(Qr_i)$, where r_i are the jump distances corresponding to the jump positions in Fig. 26 (C): $r_1 = R_{1,2}$, $r_2 = R_{1,4}$, $r_3 =$

$R_{1,5}, r_4 = R_{1,6}, r_5 = R_{1,7}, r_6 = R_{1,8}, r_7 = R_{1,9}, r_8 = R_{1,11}, r_9 = R_{1,12}, r_{10} = R_{2,5}, r_{11} =$
 $R_{2,6}, r_{12} = R_{2,8}, r_{13} = R_{2,9}, r_{14} = R_{2,12}, r_{15} = R_{3,6}, r_{16} = R_{3,9}. R_{i,j} = |\mathbf{R}_i - \mathbf{R}_j|$, where
 \mathbf{R}_i is the position of the i -th H site. The 12 equivalent H site for NH_3 and CH_3 are marked
 in Fig. 26 (C).

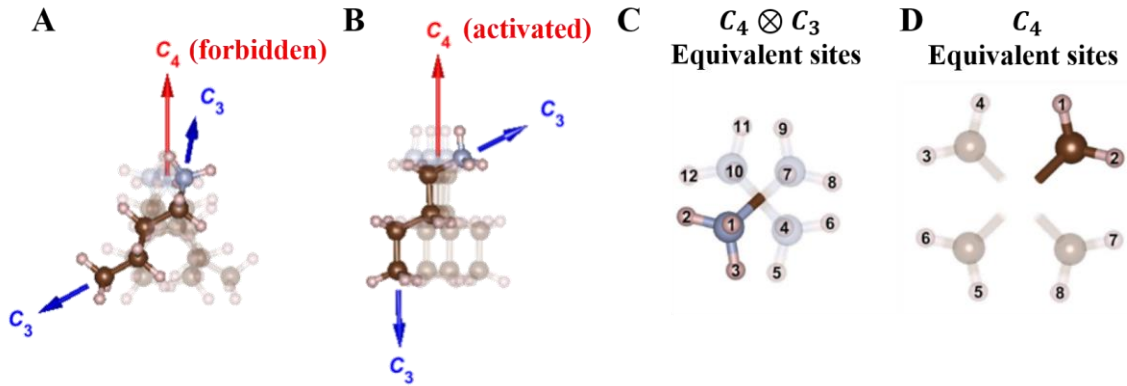


Fig. 26 Rotational modes of organic molecules in $(\text{BA})_2\text{PbI}_4$ and equivalent H sites for NH_3 , CH_3 , and CH_2 groups.

(A and B) show the rotational modes of BA^+ molecules in LT phase (A) and HT phase (B). (C) presents the 12 equivalent H sites for the $C_4 \otimes C_3$ mode of NH_3 and CH_3 groups. (D) presents the 8 equivalent H sites for the C_4 mode of CH_2 groups.

Table. S3 Model details for jump mode $\Gamma = C_4$.

Γ_γ	$\frac{1}{\tau_\gamma}$	$8 \cdot A_\gamma(Q)$
-----------------	-------------------------	-----------------------

A	0	$2 + 2j_2 + j_4 + 2j_7 + j_8$
B	$\frac{4}{\tau_{C_4}}$	$2 - 2j_2 + j_4 - 2j_7 + j_8$
E	$\frac{2}{\tau_{C_4}}$	$4 - 2j_8$

Here j_i represent the zeroth spherical Bessel function $j_0(Qr_i)$, where r_i are the jump distances corresponding to the jump positions in Fig. 26 (D): $r_2 = R_{1,3}$, $r_4 = R_{1,5}$, $r_7 = R_{2,4}$, $r_8 = R_{2,6}$. $R_{i,j} = |\mathbf{R}_i - \mathbf{R}_j|$, where \mathbf{R}_i is the position of the i -th H site. The 8 equivalent H site for CH_2 groups are marked in Fig. 26 (D).

For $(\text{PEA})_2\text{PbI}_4$, the C_3 mode of the NH_3 group is characterized by the point group C_3 (Table. S1). The structure factors $A_\gamma(Q)$ for $\Gamma = C_3$ is calculated in Table. S4.

Table. S4 Structure factors for jump mode $\Gamma = C_3$.

Γ_γ	$\frac{1}{\tau_\gamma}$	$9 \cdot A_\gamma(Q)$
A	0	$3 + 6j_0(Qr)$
E	$\frac{3}{\tau_{C_3}}$	$6 - 6j_0(Qr)$

$j_0(Qr)$ is the zeroth spherical Bessel function. r is the jump distance between H atoms of the NH_3 group.

Table. S5 Relaxation times τ_{C_4} and τ_{C_3} for the rotations of organic molecules in $(BA)_2PbI_4$ and $(PEA)_2PbI_4$. The values were obtained from model fitting to the QENS data. For $T < 275$ K, $\tau_{C_4} \approx \infty$ as the C_4 mode is frozen in $(BA)_2PbI_4$. $\langle u^2 \rangle$ is the mean squared displacement for the Debye-Waller factor $e^{-\langle u^2 \rangle Q^2}$. The errors in the parentheses were estimated by the least square fitting with 95% confidence.

$(BA)_2PbI_4$				$(PEA)_2PbI_4$		
T (K)	τ_{C_4} (ps)	τ_{C_3} (ps)	$\langle u^2 \rangle$ (\AA^2)	T (K)	τ_{C_3} (ps)	$\langle u^2 \rangle$ (\AA^2)
160	∞	342(10)	0.110(4)	170	588(90)	0.067(4)
180	∞	201(4)	0.108(3)	190	497(66)	0.073(4)
200	∞	104(2)	0.116(3)	210	408(50)	0.079(4)
220	∞	87(2)	0.104(3)	230	243(20)	0.087(4)
240	∞	70(2)	0.122(4)	250	177(12)	0.095(4)
260	∞	45(1)	0.156(3)	270	125(7)	0.103(3)
280	60(3)	6.8(2)	0.085(2)	290	92(5)	0.110(3)
300	25(2)	3.5(2)	0.082(3)	310	71(4)	0.118(3)

C₃ jump distances in CH₃ and NH₃ groups

Based on the refinement of the neutron diffraction data, the average C₃ jump distance of CH₃ is $r_c = 1.568$ Å and that of NH₃ is $r_n = 1.454$ Å. In all our calculations, we used the average jump distance $\bar{r} = \frac{r_c + r_n}{2}$. Then r_c and r_n can be written as $r_c = \bar{r} + \Delta$,

$r_n = \bar{r} - \Delta$, where $\frac{\Delta}{\bar{r}} \approx 3.8\%$. The Q -dependence of $S(Q, \hbar\omega)$ has a functional form of the l th spherical Bessel function, $j_l(Qr)$. The difference between using two separate jump distances, r_c and r_n , and using the average jump distance, \bar{r} , is minimal:

$$j_l(Q\bar{r}) - \frac{j_l(Q(\bar{r} + \Delta)) - j_l(Q(\bar{r} - \Delta))}{2} \approx \frac{1}{2} j_l''(Q\bar{r}) Q^2 \Delta^2$$

(Eq. 40)

Since $\left(\frac{\Delta}{\bar{r}}\right)^2 \approx 0.1\%$, the effect of the difference is negligible within the experimental uncertainty.

Appendix 4.

Rotational contribution estimations

We applied the rotational model to fit the elastic channel data. Fig. 27 shows the results of the fitting for four different temperatures, and the fitted parameters were listed in Table. S6.

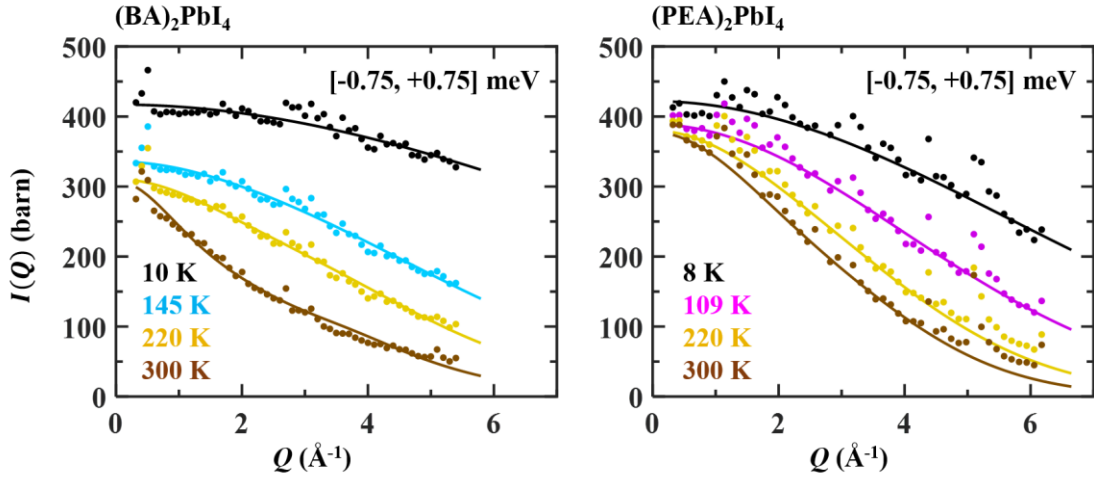


Fig. 27 Temperature dependent elastic channel data in rotational contribution estimation. The colored dots show $\hbar\omega$ -integrated neutron scattering intensity, $I(Q)$, for both samples at 4 selected temperatures with $-0.75 \leq \hbar\omega \leq 0.75$ meV with $E_i = 30$ meV. The colored solid lines are the rotational contributions at the corresponding temperatures, obtained from the fitting to the jump model described in the text. The larger Q range of $E_i = 30$ meV than $E_i = 10$ meV enhances the fitting reliability.

Table. S6 Estimated relaxation times and the mean squared displacement for the rotations of organic molecules in (BA)₂PbI₄ and (PEA)₂PbI₄ that are extracted from the model fitting to the elastic channel data as discussed in the text. Values in the parentheses indicate their errors.

(BA) ₂ PbI ₄				(PEA) ₂ PbI ₄		
<i>T</i> (K)	τ_{C_4} (ps)	τ_{C_3} (ps)	$\langle u^2 \rangle$ (Å ²)	<i>T</i> (K)	τ_{C_3} (ps)	$\langle u^2 \rangle$ (Å ²)
10	∞	∞	0.008(1)	8	∞	0.016(1)
50	∞	∞	0.010(1)	49	∞	0.021(1)
100	∞	∞	0.018(2)	109	∞	0.032(1)
145	∞	68(50)	0.026(1)	150	∞	0.039(2)
170	∞	30(20)	0.031(1)	170	∞	0.046(2)
190	∞	18(8)	0.034(2)	190	46(30)	0.051(1)
220	∞	10(4)	0.035(1)	211	17(10)	0.055(1)
250	∞	4(1)	0.049(2)	250	8(3)	0.063(2)
300	7(3)	2(1)	0.059(3)	300	4(1)	0.073(2)

References

1. Y. Tokura and N. Nagaosa. Orbital physics in transition-metal oxides. *Science* **288**, 462 (2000)
2. Y. Kamihara et al. Iron-based layered superconductor $\text{La}[\text{O}_{1-x}\text{F}_x]\text{FeAs}$ ($x=0.05-0.12$) with T_c 26 K. *J. Am. Chem. Soc.* **130**, 3296 (2008)
3. E. Dagotto and Y. Tokura. Strongly correlated electronic materials: present and future. *MRS Bulletin* **33**, 1037-1045 (2008)
4. J. Hubbard. Electron correlations in narrow energy bands. *Proceedings of the Royal Society of London* **276** (1365), 238-257 (1963)
5. E. Pavarini, E. Koch, R. Scalettar, and R. Martin (eds.). *The Physics of Correlated Insulators, Metals, and Superconductors Modeling and Simulation*. Vol. 7. Forschungszentrum Julich, 2017
6. C. Lacroix, et al. *Introduction to Frustrated Magnetism* (Springer, 2011)
7. G. H. Wannier. Antiferromagnetism. The triangular Ising net. *Phys. Rev.* **79**, 357-364 (1950)
8. L. Savary and L. Balents. Disorder-induced quantum spin liquid in spin ice pyrochlores. *Phys. Rev. Lett.* **118**, 087203 (2017)
9. H. Kawamura and K. Uematsu. Nature of the randomness-induced quantum spin liquids in two dimensions. *Journal of Physics: Condensed Matter.* **31**, 504003 (2019)
10. H. Kawamura, et al. Quantum spin-liquid behavior in the spin-1/2 random-bond Heisenberg antiferromagnet on the Kagome lattice. *J. Phys. Soc. Jpn.* **83**, 103704 (2014)
11. K. Uematsu and H. Kawamura. Randomness-induced quantum spin liquid behavior in the $s=1/2$ random J_1 - J_2 Heisenberg antiferromagnet on the Honeycomb lattice. *J. Phys. Soc. Jpn.* **86**, 044704 (2017)
12. K. Watanabe, et al. Quantum spin-liquid behavior in the spin-1/2 random Heisenberg antiferromagnet on the triangular lattice. *J. Phys. Soc. Jpn.* **83**, 034714 (2014)
13. L. Balents. Spin liquids in frustrated magnets. *Nature* **464**, 11 (2010)
14. P. W. Anderson. Resonating valence bonds: a new kind of insulator. *Mater. Res. Bull.* **8**, 153-160 (1973)

15. P. W. Anderson. The resonating valence bond state in La_2CuO_4 and superconductivity. *Science* **235**, 1196-1198 (1987)
16. V. Kalmeyer and R. B. Laughlin. Equivalence of the resonating-valence-bond and fractional quantum Hall states. *Phys. Rev. Lett.* **59**, 2095-2098 (1987)
17. X. G. Wen. Vacuum degeneracy of chiral spin states in compactified space. *Phys. Rev. B* **40**, 7387 (1989)
18. S. A. Kivelson, et al. Topology of the resonating valence-bond state: solitons and high- T_c superconductivity. *Phys. Rev. B* **35**, 8865 (1987)
19. X.-G. Wen. Zoo of quantum-topological phases of matter. *Rev. Mod. Phys.* **89**, 041004 (2017)
20. U. Geiser, et al. Superconductivity at 2.8 K and 1.5 kbar in κ -(BEDT-TTF) $_2\text{Cu}_2(\text{CN})_3$: the first organic superconductor containing a polymeric copper cyanide anion. *INorg. Chem.* **30**, 2586-2588 (1991)
21. S. Yamashita, et al. Thermodynamic properties of a spin-1/2 spin-liquid state in a κ -type organic salt. *Nat. Phys.* **4**, 459-462 (2008)
22. B. J. Powell and R. H. McKenzie. Quantum frustration in organic Mott insulators: from spin liquids to unconventional superconductors. *Rep. Prog. Phys.* **74**, 056501 (2011)
23. C. Broholm, et al. Quantum spin liquids. *Science* **367**, eaay0668 (2020)
24. M. R. Norman. Herbertsmithite and the search for the quantum spin liquid. *Rev. Mod. Phys.* **88**, 041002 (2016)
25. Y.-H. Han, et al. Fractionalized excitations in the spin-liquid state of a kagome-lattice antiferromagnet. *Nature* **492**, 406-410 (2012)
26. M. Fu, et al. Evidence for a gapped spin-liquid ground state in a kagome Heisenberg antiferromagnet. *Science* **350**, 655-658 (2015)
27. T.-H. Han, et al. Correlated impurities and intrinsic spin-liquid physics in the kagome material herbertsmithite. *Phys. Rev. B* **94**, 060409 (2016)
28. A. Banerjee, et al. Neutron scattering in the proximate quantum spin liquid α - RuCl_3 . *Science* **356**, 1055-1059 (2017)
29. S. M. Winter, et al. Breakdown of magnons in a strongly spin-orbital coupled magnet. *Nat. Commun.* **8**, 1152 (2017)

30. K. X. Steirer, et al., Defect tolerance in methylammonium lead triiodide perovskite. *ACS Energy Lett.* **2**, 360-366 (2016)
31. Y. Chen and H. Zhou. Defects chemistry in high-efficiency and stable perovskite solar cells. *Journal of Applied Physics* **128**, 060903 (2020)
32. M. A. Green, et al.. Solar cell efficiency tables (Version 55). *Prog. Photovoltaics* **28**, 3-15 (2020)
33. S. T. Zhang, et al. Efficient red perovskite light-emitting diodes based on solution-processed multiple quantum wells. *Adv. Mater.* **29**, 1606600 (2017)
34. B. Traore, et al. Composite nature of layered hybrid perovskites: assessment on quantum and dielectric confinements and band alignment. *ACS Nano* **12**, 3321-3332 (2018)
35. C. Katan, et al. Quantum and dielectric confinement effects in lower-dimensional hybrid perovskite semiconductors. *Chem. Rev.* **119**, 3140-3192 (2019)
36. N. N. Wang, et al. Perovskite light-emitting diodes based on solution-processed self-organized multiple quantum wells. *Nat. Photonics* **10**, 699-704 (2016)
37. X. Gong, et al. Electron-phonon interaction in efficient perovskite blue emitters. *Nature Materials* **17**, 550-556 (2018)
38. Z. F. He, et al. High-efficiency red light-emitting diodes based on multiple quantum wells of phenylbutylammonium-cesium lead iodide perovskites. *ACS Photonics* **6**, 587-594 (2019)
39. G. L. Squires. *Introduction to the Theory of Thermal Neutron Scattering* (Cambridge 1996).
40. M. Bee, *Quasielastic Neutron Scattering: Principles and Applications in Solid State Chemistry, Biology and Materials Science*. Bristol and Philadelphia: Adam Hilger, 1988.
41. G. Xu, et al. Absolute cross-section normalization of magnetic neutron scattering data. *Review of Scientific Instruments* **84**, 083906 (2013)
42. Y. Xu, et al. Comparative description of magnetic interactions in Sr₂CuTeO₆ and Sr₂CuWO₆. *J. Phys.: Condes. Matter* **29**, 105801 (2017)
43. T. Koga, et al. Magnetic structure of the S=1/2 quasi-two-dimensional square-lattice Heisenberg antiferromagnet Sr₂CuTeO₆. *Phys. Rev. B* **93**, 054426 (2016)

44. O. Mustonen, et al. Tuning the $S=1/2$ square-lattice antiferromagnet $\text{Sr}_2\text{Cu}(\text{Te}_{1-x}\text{W}_x)\text{O}_6$ from Nèel order to quantum disorder to columnar order. *Phys. Rev. B* **98**, 064411(2018)
45. S. Vasala, et al. Magnetic structure of Sr_2CuWO_6 . *J. Phys.: Condes. Matter* **26**, 496001 (2014)
46. P. Babkevich, et al. Magnetic excitations and electronic interactions in $\text{Sr}_2\text{CuTeO}_6$: a spin-1/2 square lattice Heisenberg antiferromagnet. *Phys. Rev. Lett.* **117**, 237203 (2016)
47. H. C. Walker, et al. Spin wave excitations in the tetragonal double perovskite Sr_2CuWO_6 . *Phys. Rev. B* **94**, 064411 (2016)
48. O. Mustonen, et al. Spin-liquid-like state in a spin-1/2 square-lattice antiferromagnet perovskite induced by d^{10} - d^0 cation mixing. *Nature Communications* **9**:1085 (2018)
49. M. Watanabe, et al. Valence-bond-glass state with a singlet gap in the spin-1/2 square-lattice random J_1 - J_2 Heisenberg antiferromagnet $\text{Sr}_2\text{CuTe}_{1-x}\text{W}_x\text{O}_6$. *Phys. Rev. B* **98**, 054422 (2018)
50. G. Ehlers, et al. The new cold neutron chopper spectrometer at the Spallation Neutron Source: Design and performance. *Rev. Sci. Instrum.* **82**, 085108 (2011)
51. G. E. Granroth, et al. SEQUOIA: a newly operating chopper spectrometer at the SNS. *Journal of Physics: Conference Series* **251**, 12058 (2010)
52. X. Hu, et al. Freezing of a disorder induced spin liquid with strong quantum fluctuations. *Phys. Rev. Lett.* **127**, 017201 (2021)
53. I. A. Zaliznyak and S.-H. Lee. *Neutron scattering with 3-Axis spectrometer* in Modern Techniques for Characterizing Magnetic Materials. (Boston, 2004)
54. S. Ji, et al. Orbital order and partial electronic delocalization in a triangular magnetic metal Ag_2MnO_2 . *Phys. Rev. B* **81**, 094421 (2010)
55. J. A. Mydosh. *Spin glasses: an experimental introduction*. Taylor & Francis (1993)
56. V. M. Katukuri, et al. Exchange interactions mediated by non-magnetic cations in double perovskites. *Phys. Rev. Lett.* **124**, 077202 (2020)
57. M. Tarzia and G. Biroli. The valence bond glass phase. *Europhys. Lett.* **82**, 67008 (2008)
58. R. R. P. Singh. Valence bond glass phase in dilute kagome antiferromagnets. *Phys. Rev. Lett.* **104**, 177203 (2010)
59. B. I. Halperin and W. M. Saslow. Hydrodynamic theory of spin waves in spin glasses and other systems with noncollinear spin orientations. *Phys. Rev. B* **16**, 2154 (1977)

60. D. Podolsky and Y. B. Kim. Halperin-Saslow modes as the origin of the low-temperature anomaly in NiGa₂S₄. *Phys. Rev. B* **79**, 140402 (2009)
61. I. Klich, S.-H. Lee, and K. Iida. Glassiness and exotic entropy scaling induced by quantum fluctuations in a disorder-free frustrated magnet. *Nat Commun.* **5**, 3497 (2014)
62. A. Samarakoon *et al.* Aging, memory, and nonhierarchical energy landscape of spin jam. *PNAS* **113**, 11806 (2016)
63. C. C. Stoumpos *et al.* Ruddlesden-Popper hybrid lead iodide perovskite 2D homologous semiconductors. *Chemistry of Materials* **28**(8): p. 2852-2867 (2016)
64. R. Kajimoto *et al.* The Fermi chopper spectrometer 4SEASONS at J-PARC. *Journal of the Physical Society of Japan* **80**(Suppl. B): p. SB025 (2011)
65. K. Nakajima *et al.* AMATERAS: a cold-neutron disk chopper spectrometer. *Journal of the Physical Society of Japan* **80**(Suppl. B): p. SB028 (2011)
66. G. Kresse and J. Furthmüller. Efficient iterative schemes for ab initio total-energy calculations using a plane-wave basis set. *Phys. Rev. B* **54**(16): p. 11169 (1996)
67. J. P. Perdew, K. Burke, and M. Ernzerhof. Generalized gradient approximation made simple. *Phys. Rev. Lett.* **77**(18): p. 3865 (1996)
68. D. Zhang. (2019) Crystal structures, rotational, vibrational dynamics, and optoelectronic properties of two-dimensional hybrid organic-inorganic perovskites. Ph. D thesis. University of Virginia. <https://doi.org/10.18130/v3-mddw-1t50>.
69. K. Du *et al.* Two-dimensional lead(II) halide-based hybrid perovskites templated by acene alkylamines: crystal structures, optical properties, and piezoelectricity. *Inorg. Chem.* **56**, 9291-9302 (2017)
70. Y. Q. Cheng *et al.*, Simulation of inelastic neutron scattering spectra using OCLIMAX. *Journal of Chemistry Theory and Computation* **15**, 1974-1982 (2019)
71. T. Chen *et al.*, Rotational dynamics of organic cations in the CH₃NH₃PbI₃ perovskite. *Phys. Chem. Chem. Phys.* **17**, 31278-31286 (2015)
72. K. Miyata, T. L. Atallah, and X. Y. Zhu, Lead halide perovskites: Crystal-liquid duality, phonon glass electron crystals, and large polaron formation. *Sci. Adv.* **3**, e1701469 (2017).
73. G. Xing *et al.*, Long-range balanced electron- and hole-transport lengths in organic-inorganic CH₃NH₃PbI₃, *Science* **342**, 344 (2013).

74. Q. Dong et al., Electron-hole diffusion lengths >175 μm in solution-grown $\text{CH}_3\text{NH}_3\text{PbI}_3$ single crystals, *Science* **347**, 967 (2015).
75. D. Shi et al., Low trap-state density and long carrier diffusion in organolead trihalide perovskite single crystals, *Science* **347**, 519 (2015).
76. L. M. Herz, Charge-carrier dynamics in organic-inorganic metal halide perovskites, *Annu. Rev. Phys. Chem.* **67**, 65 (2016).
77. T. Leijtens et al., Carrier trapping and recombination: The role of defect physics in enhancing the open circuit voltage of metal halide perovskite solar cells, *Energy Environ. Sci.* **9**, 3472 (2016).
78. X. Y. Zhu and V. Podzorov, Charge carriers in hybrid organic-inorganic lead halide perovskites might be protected as large polarons, *J. Phys. Chem. Lett.* **6**, 4758 (2015).
79. K. Miyata et al., Large polarons in lead halide perovskites, *Sci. Adv.* **3**, e1701217 (2017).
80. K. Miyata and X. Y. Zhu, Ferroelectric large polarons, *Nat. Mater.* **17**, 379 (2018).
81. F. Zheng and L.-W. Wang, Large polaron formation and its effect on electron transport in hybrid perovskite, *Energy Environ. Sci.* **12**, 1219 (2019).
82. J. M. Frost, L. D. Whalley, and A. Walsh, Slow cooling of hot polarons in halide perovskite solar cells, *ACS Energy Lett.* **2**, 2647 (2017).
83. T. Chen et al., Origin of long lifetime of band-edge charge carriers in organic-inorganic lead iodide perovskites, *PNAS* **114**, 7519 (2017).
84. D. Cortecchia et al., Polaron self-localization in white-light emitting hybrid perovskites, *J. Mater. Chem. C* **5**, 2771 (2017).
85. A. J. Neukirch et al., Polaron stabilization by cooperative lattice distortion and cation rotations in hybrid perovskite materials, *Nano Lett.* **16**, 3809 (2016).
86. A. D. Wright et al., Electron-phonon coupling in hybrid lead halide perovskites, *Nat. Commun.* **7**, 11755 (2016).
87. S. Tombe et al., Optical and electronic properties of mixed halide (X = I, Cl, Br) methylammonium lead perovskite solar cells, *J. Mater. Chem. C* **5**, 1714 (2017).
88. K. Wu et al., Temperature-dependent excitonic photoluminescence of hybrid organometal halide perovskite films, *Phys. Chem. Chem. Phys.* **16**, 22476 (2014).

89. Z. Guo et al., Electron-phonon scattering in atomically thin 2D perovskites, *ACS Nano* **10**, 9992 (2016).
90. O. Yaffe et al., Local polar fluctuations in lead halide perovskite crystals, *Phys. Rev. Lett.* **118**, 136001 (2017)
91. D. Zhang, X. Hu, et al., Temporally decoherent and spatially coherent vibrations in metal halide perovskites. *Phys. Rev. B* **102**, 224310 (2020)
92. H. Kim et al., Direct observation of mode-specific phonon-band gap coupling in methylammonium lead halide perovskites, *Nat. Commun.* **8**, 687 (2017)
93. H. Zhu et al., Organic cations might not be essential to the remarkable properties of band edge carriers in lead halide perovskites. *Adv. Mater.* **29**, 1603072 (2016)